Microscale Modeling of Porous Thermal Protection System Materials

A THESIS

SUBMITTED TO THE FACULTY OF THE GRADUATE SCHOOL

OF THE UNIVERSITY OF MINNESOTA

BY

Eric C. Stern

IN PARTIAL FULFILLMENT OF THE REQUIREMENTS

FOR THE DEGREE OF

DOCTOR OF PHILOSOPHY

Graham V. Candler

May, 2015

Acknowledgements

First and foremost, I would like to express my sincere gratitude to my advisor Graham Candler. He has provided me the space and freedom to develop my own scientific identity, and has challenged me at opportune times to probe deeper and stretch myself intellectually. He has been, and will continue to be, a role model to me for his work ethic, his integrity, and his unique instinct for pursuing research that is of value both scientifically and academically, while simultaneously having an immediate and significant impact on "real world" engineering problems. In this authors opinion, there is no one who does the latter as effectively, and he has provided me a template to strive for in my own career.

I would also like to sincerely thank Professor Tom Schwartzentruber and Dr. Ioannis Nompelis. It goes without saying that without their DSMC code, and their technical expertise, this work would not have been possible. It is a testament to their efforts that a DSMC novice such as myself was able to come in and, in a short amount of time, modify and use their code to solve complex problems.

Additionally I would like to thank the members of my dissertation committee, Professors Richard James and Stephen Girshick, for their time and expertise during both my preliminary and final defense.

To my fellow students in the Candler group, (in no particular order) Kyle Boe, Aaron Neville, Pramod Subdareddy, Ross Chaudhry, Jason Bender, Pietro Ferrero, Anand Kartha, Sriram Doraiswamy, Ross Wagnild, Matt Bartkowicz, Dave Peterson,

Steph Jensen, Vlad Gidzak, Erik Tylczak, Alan Schwing, Derek Dinzl, Loretta Treviño, and most especially Joe Brock, I would like to say an extra special thank you. All of the discussions, debates, and arguments; lunches, coffees, and wines; Risk games, and pool games have truly enriched me, and made my time in graduate school go by way too quickly.

Thank you to Claudia Meyer and the entire NSTRF team at NASA. It has been a great honor to be among the first class of this amazing fellowship program. Beyond the financial support, the opportunities this fellowship has provided me have set me on a path toward my achieving my dreams. As I continue to the reap the rewards of this tremendous opportunity, so too will I continue to be grateful to NASA and to this program.

At NASA, I would like to especially acknowledge Dr. Michael Barnhardt for his mentorship and friendship throughout my fellowship. Additionally, I would like to thank Drs. Michael Wright and Ethiraj Venkatapathy for their immeasurable contributions to my career and professional growth. Most people are lucky to have one generous mentor within their field; I have three, and I am deeply grateful.

Finally, I would like to thank my ever-supportive family. To my father Wayne, my aunt Marsha, and most of all to my mother Meg; I could not have done it without you. Thank you.

Dedication

To my mother. Thank you.

Abstract

Ablative thermal protection system (TPS) materials play a vital role in the design of entry vehicles. Most simulation tools for ablative TPS in use today take a macroscopic approach to modeling[1],[2], which involves heavy empiricism. Recent work[3] has suggested improving the fidelity of the simulations by taking a multi-scale approach to the physics of ablation. In this work, a new approach for modeling ablative TPS at the microscale is proposed, and its feasibility and utility is assessed. This approach uses the Direct Simulation Monte Carlo (DSMC) method to simulate the gas flow through the microstructure, as well as the gas-surface interaction. Application of the DSMC method to this problem allows the gas phase dynamics – which are often rarefied – to be modeled to a high degree of fidelity. Furthermore this method allows for sophisticated gas-surface interaction models to be implemented.

In order to test this approach for realistic materials, a method for generating artificial microstructures which emulate those found in spacecraft TPS is developed. Additionally, a novel approach for allowing the surface to move under the influence of chemical reactions at the surface is developed. This approach is shown to be efficient and robust for performing coupled simulation of the oxidation of carbon fibers.

The microscale modeling approach is first applied to simulating the steady flow of gas through the porous medium. Predictions of Darcy permeability for an idealized microstructure agree with empirical correlations from the literature, as well as with predictions from computational fluid dynamics (CFD) when the continuum assumption is valid. Expected departures are observed for conditions at which the continuum assumption no longer holds. Comparisons of simulations using a fabricated microstructure to experimental data for a real spacecraft TPS material show good agreement when similar microstructural parameters are used to build the geometry.

The approach is then applied to investigating the ablation of porous materials through oxidation. A simple gas surface interaction model is described, and an approach for coupling the surface reconstruction algorithm to the DSMC method is outlined. Simulations of single carbon fibers at representative conditions suggest this approach to be feasible for simulating the ablation of porous TPS materials at scale. Additionally, the effect of various simulation parameters on in-depth morphology is investigated for random fibrous microstructures.

Contents

List of Tables

List of Figures

Chapter 1

Ablative Thermal Protection System Modeling

This chapter provides an introduction to the state-of-the-art in the modeling of the ablative materials used in entry vehicles. The first part will give an overview on the typical models in use for engineering applications as of this writing. Then some background on previous efforts into microscale modeling will be provided.

1.1 Introduction

Spacecraft thermal protection systems (TPS) must endure extreme aerothermal environments during atmospheric entry. There are many different TPS architectures depending on the application, however most often on the forebody of the vehicle, an ablative TPS material is used. Furthermore ablative TPS materials remain the only materials applicable for ballistic entry. The central idea behind these materials is to relieve the heating to the vehicle through sacrificial removal of the material. Figure 1.1 shows a section of a core sample taken from the Stardust sample return capsule [14],[15]. Stardust was – at the time of its entry – the fastest human-made object to pass through the atmosphere with a velocity of about 12.6 km/s. The heat shield for the entry vehicle was made of

the Phenolic Impregnated Carbon Ablator (PICA) [16] material.

Figure 1.1: Image of a core of PICA material taken from the Stardust sample return vehicle [4].

Pyrolyzing ablators such as PICA are typically composed of a rigid refractory porous medium, which is impregnated with an organic resin. In the case of PICA, the porous medium is composed of carbon fibers. A Scanning Electron Micrograph (SEM) performed under the current work of the carbon fibers used in PICA can be seen in fig. 1.2.

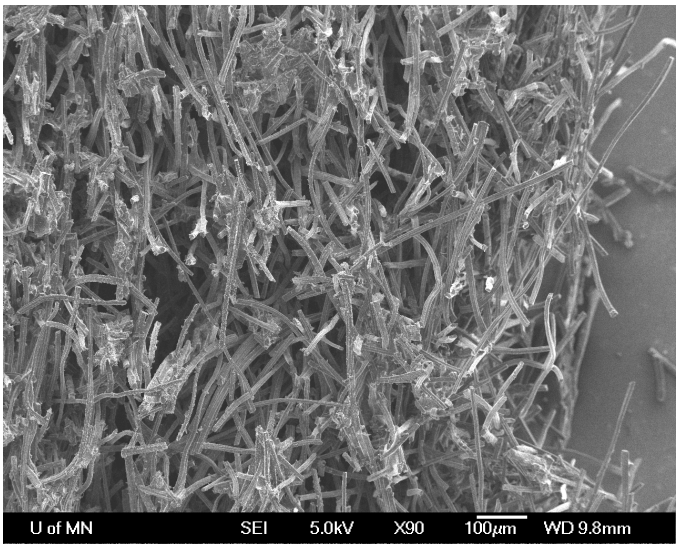

Figure 1.2: Scanning electron micrograph of the FiberForm material used in PICA.

As the material is heated during entry, the phenolic decomposes and the gas produced by the pyrolysis is blown out through the porous medium and into the flow of gas around the vehicle. As the material is heated still further, the carbon fibers themselves are ablated from near the surface. Figure 1.3 shows a schematic of this process for a PICA-like material.

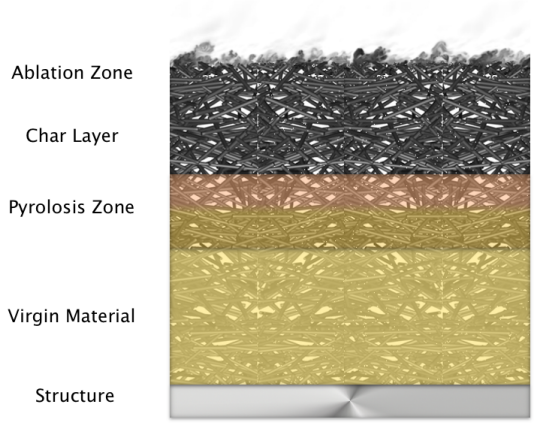

Figure 1.3: Schematic of a typical pyrolyzing ablator.

There are a number of processes and effects during the ablation process which produce a desirable relief of the heat load delivered to the vehicle. First the chemical decomposition of the resin is typically endothermic, thereby taking energy from the flowfield change the phase of the resin and break its chemical bonds. Furthermore, the ablation of the carbon reinforcement may also consume energy, particularly when the temperatures are such that the material may sublime. Mechanical ablation through erosion of the fibrous structure can also serve to relieve heating by transporting heated material near the surface downstream and into the wake of the vehicle. Finally, the blowing of pyrolysis gas products into the flow serves to displace the hot boundary layer, moving it away from the vehicle, and providing further cooling effect.

As one might expect, modeling the performance and behavior of spacecraft thermal protection system (TPS) materials as they are exposed to these extreme conditions of atmospheric entry is a very complicated, challenging, and inherently multidisciplinary problem. In the next two sections, a brief overview of current modeling approaches will be given, first focusing on so called "engineering" models, followed by some recent efforts in microscale modeling.

1.2 Engineering Models

Historically, modeling of lightweight ablative TPS materials began in the 1960's during the Apollo program. One of the early computer codes which would end up being the primary influence on virtually all modeling tools for spacecraft applications to come was the Charring Materials Thermal Response and Ablation (CMA) code [17], [18]. This code could solve for the thermal and ablative response of materials such as that seen in fig. 1.3. The approach taken was to model the in-depth decomposition of the solid, the in-depth thermal transport, and a surface energy balance. Later, a version of CMA with a more robust implicit time integration scheme called the Fully Implicit Ablation and Thermal (FIAT) response program was developed by Chen and Milos [1]. Both of these codes – CMA and FIAT – are one-dimensional. Extensions into two-dimensions (2-D) and three-dimensions (3-D) have been made with the Two-dimensional Implicit Thermal response And ablatioN (TITAN) [19] and 3dFIAT [20],[21], respectively.

The in-depth thermal transport equation mentioned above is largely the same across the main codes in use today, as are the decomposition equations, so they will be omitted here. The surface energy balance (SEB) is an important component in all codes and requires an assumption that will be challenged by results from the current work. The SEB is written in many forms, and can include many different terms depending on the material and level of fidelity. A simplified form of that found in typical ablator response

codes is written as:

$$\dot{q}_{cond,s} = \dot{q}_{conv} + \alpha\dot{q}_{rad} - \sigma\left(\epsilon T_w^4 - \alpha T_\infty^4\right) + \dot{m}_c h_c + \dot{m}_g h_g - \dot{m}_w h_w \tag{1.1}$$

In this equation, the individual terms - from left to right - can be explained as follows: heat flux conducted into the solid, convective heating from the flow field, radiative heating from the flow field, net re-radiation from the surface, energy flux from recession of the surface, energy flux from pyrolysis gas flowing to the surface, and energy flux due to mass transfer to the flow field. The important aspect of this equation to note is that the ablation of the char - embodied by $\dot{m}$ - is accounted for only at the surface. This assumption will be examined in greater detail in Ch. 4.

It is important to note at this point that in CMA-style codes (such as FIAT and TITAN), the flow of pyrolysis gas products through the char layer, as seen in fig.1.3, is not modeled directly. Rather, the gas is assumed to be instantly transported and removed through the fluid-surface interface. Later attempts to improve these models have often involved additional equations to account for the motion of pyrolysis gas through the char, and these shall be discussed in further detail in subsequent sections. Briefly, codes which include a model for the pyrolysis gas typically invoke some version of Darcy's Law to account for the hydrodynamic resistivity of the porous medium. There are a number of authors and codes which have implemented various models of this type. The CHarring Ablator Response (CHAR) code [22],[2] used by NASA Johnson Space Center, and developed by Amar et al. solves – in addition to the equations discussed above – a continuity equation for the pyrolysis gas. A similar approach has been taken by Martin et al. [23],[24] in their Modeling of Pyrolysis and Ablation Response (MOPAR) code. Both of these code share a similar heritage, and both use a Control Volume Finite Element Method (CVFEM) to solver the governing equations.

A typical gas continuity equation found in these code, written in conservation law

form, is as follows:

$$\frac{\partial \phi \rho_g}{\partial t} + \nabla \cdot (\phi \rho_g \mathbf{u}_g) = \dot{\omega}_g \tag{1.2}$$

Here, ρ_g is the density of the pyrolysis gas, ϕ is the porosity of the medium, u_g is the apparent velocity of the gas, and $\dot{\omega}_g$ is rate of mass production of pyrolysis gas due to decomposition of the solid. This equation introduces two new unknowns, ρ_g and u_g, but only one new equation. Therefore, to close this equation set, the gas velocity is modeled. This is most often done using Darcy's Law, which may be written in its simplest form as:

$$\mathbf{u}_g = -\frac{K}{\mu} \nabla P \tag{1.3}$$

Here, we have introduced a material specific constant, K, which is the Darcy permeability – in this case we have assumed a scalar value for K, although it may in principle be a tensor. This equation simply says that the apparent gas velocity in a porous medium is proportional to the pressure gradient. This relation was originally derived experimentally by measuring the flow of water through beds of sand, however it was later proved to be theoretically rigorous by Whitaker [25]. This equation for the gas velocity can be substituted into the continuity equation (1.2) to get the following:

$$\frac{\partial \phi \rho_g}{\partial t} - \nabla \cdot (\rho_g \frac{K}{\mu} \nabla P) = \dot{\omega}_g \tag{1.4}$$

We can make a further substitution by assuming the pyrolysis gas obeys the ideal gas law: $P = \rho_g R_g T$, which then gives us a continuity equation in terms of ρ_g and T. The temperature, T, is computed based on the in-depth thermal transport equation which is omitted here for the sake of brevity.

It should be noted that the validity of Darcy's Law requires that the flow obey certain assumptions. Most important is that the flow is microscopically in the Stokes regime. More specifically, that the Reynolds number based on the microscopic fluid velocity

and the mean pore diameter is much less than unity. There have been modifications to Darcy's Law that are meant to account for higher Reynolds number effects. Martin and Boyd [26] investigated use of Forchheimer's Law, a modification to Darcy's Law which is meant to account for *inertial* effects at the pore scale. One of the issues with this approach is that it adds another coefficient, which in general must be experimentally determined.

Further efforts have been made to add more fidelity by modeling the momentum transport within the porous medium as a separate equation. Perhaps one of the first examples of this is the work of Ahn and Park[27]. In their work, they add a momentum transport equation to the energy transport, gas continuity, and solid decomposition equations discussed above. More recently, Weng and Martin[28] as well as Chen and Milos[29] have used a similar approach. In both cases the authors use Darcy's and Forchheimer's Laws to account for the resistance of the porous medium to the gas flow. This is done by including these two laws as "sink" terms in the momentum equation.

It is the opinion of this author at the time of this writing that approaches to modeling the pyrolysis gas momentum transport – whether by a Darcy closure of the gas continuity equation, or of the gas momentum equation – have yet to yield an increase in the fidelity of material response predictions. This may be due in part to the fact that, as mentioned above, all of these models require empirical coefficients that must typically be determined experimentally, and are often based on limited data. Furthermore, there may be questions as to the validity of invoking Darcy's law under these conditions. One of the aims of this is work to provide a means for numerically determining these coefficients, which will be described in Chapter 3, as well as provide a framework for assessing the validity of Darcy's law under transient conditions and aiding in the development of future models.

1.3 Microscale Modeling of Ablation

Thus far, the models discussed have all been of the volume-averaged variety, meaning that they assume a continuous medium, and the effects of the microscopic irregularity of the medium are *modeled*. Recently, some researchers have taken the approach of modeling the materials at the microscale in order to gain insight into the complex phenomena occurring in-depth, as well as to inform the closures found in the volume-averaged models.

Much of the early numerical effort in this area was performed by research groups in France who were primarily concerned with modeling the onset of surface roughness due to ablation within rocket nozzles [30],[31],[32]. For these studies, a random walk algorithm developed by Vignoles[33] was used to model the diffusion of reactant species to the ablative surface. This approach was later refined and extended to three-dimensions by Lachaud and Vignoles[5]. For these studies, the gas-surface interaction is modeled by a sticking coefficient coupled to a simplified marching cubes algorithm[34] for moving and tracking the gas-surface interface. A sketch of the random walk ablation techniques, taken from [5], can be see in fig. 1.4.

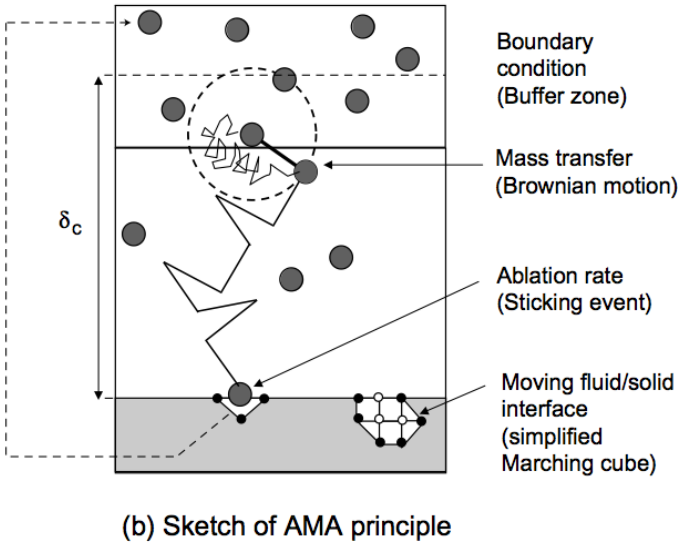

Figure 1.4: Illustration of the brownian motion technique employed by Lachaud et. al, from [5].

It has been shown by Einstein[35] that the diffusion of a random walker due to Brownian motion can be related to the Fickian diffusion coefficient for single species. This random walk approach has been more recently applied to porous thermal protection system materials used in entry spacecraft applications by Lachaud et al.[3]. Their work was able to reproduce some expected morphologies for a PICA-like ablative material, as seen in fig. 1.5 taken from [3] . One can see in this figure that the resin matrix has recessed, and there is some thinning of the fibers near the surface. More importantly, they showed that under certain conditions the ablation of the carbon reinforcement occurred in-depth, and *not* just at the surface. Recall that most engineering material response models treat ablation as a surface phenomenon. It was suggested by Lachaud et al. in this paper that future engineering response models should account for volumetric ablation occurring in-depth. This idea has begun to be explored by Martin[36], who has proposed a volume averaged ablation model which accounts for the oxidation of

cylindrical fibers. At the time of this writing, work is on-going toward validating this type of model using flow-tub oxidation experiments [10].

Figure 1.5: Simulation of a PICA-like pyrolyzing ablator from [6].

One of the main limitations of the microscale modeling approach taken by Lachaud et al. is that it is only rigorous for single component diffusion. This is due to fundamental assumptions underlying the Brownian motion technique. Therefore its utility is mostly confined to uncovering some broad physical phenomena – such as the volumetric ablation idea – but will be extremely limited in its ability to simulate a realistic system. The real system will include, among other things, many chemical species in the gas phase which may react with one another. Additionally, the random walk approach is not able to model convection, and therefore will not yield insight into the problems of porous media flow detailed in the previous section. One of the primary objectives of the current work is to address some of these limitations in the physical modeling.

Another aspect of this problem that was well-documented by Lachaud et al. [3] was that the flow within the porous medium is often rarefied. The extent to which a flow

is rarefied is typically described by the Knudsen number, which is defined as the ratio between the mean free path of the gas to a characteristic length scale ($Kn = \lambda/L$). Typically when the Knudsen number is greater than approximately 0.1 the Navier-Stokes equations, which are based on a continuum assumption, are no longer valid. In the case of a porous ablator, the small length scales (fibers diameters are typically in the range of 1 to 10μm) that occur in the denominator of the Knudsen number are what are responsible for the rarefied nature of the microscopic flow. Additionally, low pressures in the early part of a entry trajectory while the spacecraft is still in the upper atmosphere may result in further rarefication. An illustration of the Knudsen numbers encountered by the heatshield for the Stardust entry vehicle discussed previous was given by Lachaud et al. [3] and is shown in fig. 1.6. We can see from this plot that the lowest Knudsen number (most continuum) encountered by the material was > 0.02, and that the majority of the time, it is well within the transitional regime ($0.1 < Kn < 100$). This suggests that modeling these flows will require a method which can account for a range of Knudsen numbers, and be particularly effective in more rarefied regimes.

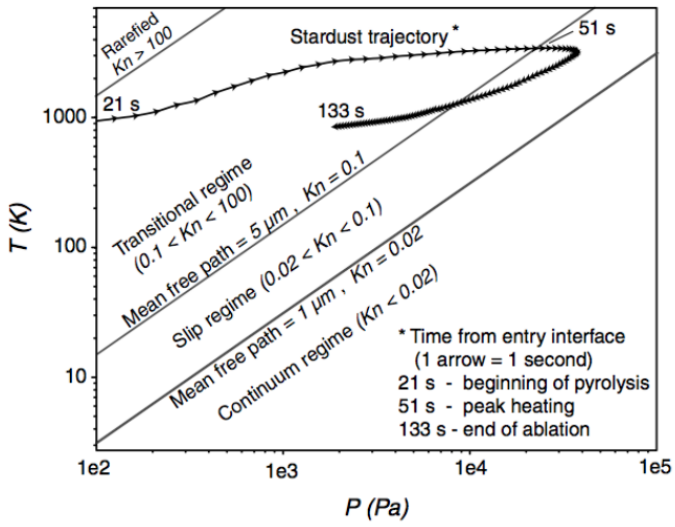

Figure 1.6: Plot showing flow regimes encountered within the TPS of the Stardust entry vehicle [3]

In order to address some of the aforementioned limitations with the previous work on microscale modeling, the current work employs the Direct Simulation Monte Carlo (DSMC) method to model the gas phase, and gas-surface interaction phenomena. DSMC is a stochastic particle based method, which is valid (given sufficient computational resources) for all Knudsen numbers. Additionally, the method inherently handles convection, as well as many other physical phenomena that may need to be accounted for.

1.4 Scope of this Work

The primary objective of this work is to develop a framework for performing simulations of porous spacecraft TPS materials at the microscale, and to apply this framework to simple case studies to assess its viability, as well its utility for informing macroscopic models. Within the context of the pyrolyzing ablator (such as the one seen in fig. 1.3)

the simulations presented in the current work can be thought of as focusing exclusively on the "char layer."

- Chapter 2 will provide an overview of the methodologies employed in this study. It will begin with a brief introduction to the DSMC method, as well as the specific code that is used in this work. Enhancements to the code specific to this work will then be detailed. Additionally, the procedures used to generate artificial microstructures is outlined. Finally, a new method for moving the fiber-fluid interface is proposed.

- Chapter 3 will focus on the application of the method to characterizing the permeability of porous materials. Here the DSMC method's ability to simulate gas convection will be leveraged. Validation and verification simulations are performed on idealized microstructures.

- Chapter 4 will focus on the application of the proposed methodology to ablating microstructures. Here, the surface movement algorithm proposed in Ch. 2 will be applied. The effect of the variation of various simulation parameters on the evolution of the microstructure

- Chapter 5 will summarize the conclusions from the current work and address some potential avenues for future work.

Chapter 2

Methodology

This chapter focuses on the methods used to study the ablation of porous spacecraft TPS at the microscale. It begins with a brief overview of the DSMC method, as well as the specific implementation used for this work. Modifications made to this code to properly model subsonic boundary conditions are detailed. In addition to the discussion related to DSMC, the method for generating microstructures, as well as for allowing the surfaces to move are discussed.

2.1 The Direct Simulation Monte Carlo Method

The Direct Simulation Monte Carlo (DSMC) method originated with G. A. Bird [37]. It is a particle method which directly solves for the motion and collisions of gas particles in a flow. The DSMC method differs from Molecular Dynamics (MD) approaches in that the collisions between particles are treated stochastically, while the particle trajectories are treated deterministically in both methods. The other most significant difference between DSMC and deterministic approaches is that particles in a simulation typically represent a large number of actual molecules, atoms, charged particles, etc.. These two aspects of the method combined make DSMC simulations much less computationally expensive than MD simulations. However the underlying assumptions in DSMC place

certain requirements on the size of the grid cells that are used for sorting of particles, as well as on the time step over which the particle trajectories are integrated. Specifically, the grid cells in the computationally mesh must be on the order of the mean free path of the gas, and the time step must be on the order of the mean collision time of the gas.

It has been shown that the DSMC method produces solutions to the Boltzmann equation [38], which can describe the transport processes in a gas in non-equilibrium [39] and is valid for all Knudsen number that are of interest for entry modeling applications. Because the DSMC method imposes the requirement that grid cells be on the order of the mean free path, it has primarily heretofore been applied to the simulation of rarefied flows. These are flows in which the Knudsen number is large. Most often these applications have been centered on the simulating high velocity flow fields around vehicles in the upper atmosphere where the density is low, and therefore the Knudsen number is high due to the mean free path despite the length scales being potentially large. For the applications to be discussed in the current work, the gas densities may not be too low, however the small length scales involved give rise to high Knudsen numbers. Because the Knudsen number scales roughly with the density of the gas, The computational cost of a three-dimensional DSMC calculation scales roughly with the cube of the density. Based on this, one can see how the cost of a DSMC simulation quickly becomes intractable as the Knudsen number goes into the continuum regime. Navier-Stokes solvers, by contrast, are indifferent to the density, though they are not valid for high Knudsen numbers.

As the speed and availability of computational resources increases, the potential to apply DSMC to lower Knudsen number problems increases. There have been several notable efforts into parallelization of the DSMC method. Perhaps most notable are the work of LeBeau [40], as well as Dietrich and Boyd[41].

2.1.1 MGDS

The DSMC flow solver used for this work is the Molecular Gas Dynamic Simulator (MGDS) code[42],[43], developed at the University of Minnesota. The MGDS code is a parallel implmentation of Bird's method, and has a number of desirable features for simulating the types of flow which are of interest in the current study. One of the advantages to using DSMC, and this code in particular, is the ability to handle complicated geometries. The cutcell algorithm[7] developed for the MGDS code has proven to be very robust. Figure 2.1 shows the surface mesh and cartesian cutcell grid from an *MGDS* simulation of the MIR space station from [7]. This figure illustrates the attractive feature that one can go directly from a CAD model of a surface directly to simulation. This is contrast to CFD where often times a great deal of user expertise is required to generate a volume grid, and very complicated or detailed geometries – such as that in Fig. 2.1 – would be intractable. This feature is leveraged throughout the current work, and the robustness in particular will be demonstrated in Chapter 5 when it is applied to simulating *real* microstructures obtained from X-ray computed microtomography.

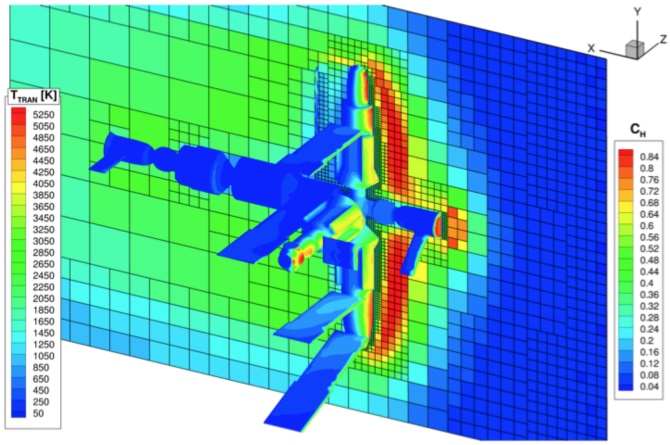

Figure 2.1: Simulation of the MIR space station using the *MGDS* code [7] illustrating the cutcell algorithm.

A second feature of the DSMC approach which makes it attractive for performing microscale simulations of ablative TPS materials is relative straight-forwardness of the boundary condition implementation. For DSMC, the treatment of the boundaries requires less abstraction than for continuum approaches. Typically, continuum approaches such as CFD require an assumption of equilibrium near the surface in order to define a continuum flux. In DSMC, no such assumption is required. In principal, one can define their gas-surface interaction model in terms of the state of the impacting gas particle, or of the surface in a straight-forward manner. For the present work, the implementation in *MGDS* made the gas-surface interaction model to be detailed in Chapter 4 very straightforward, and facilitates the future implementation of more sophisticated gas-surfaec interaction models.

2.1.2 Subsonic Boundary Conditions

Low-speed flows, which are of interest in the current work, pose some challenges to the DSMC method. This is in-part due to the fact that the most probable velocity for a gas particle is typically very large compared to the mean flow velocity. From kinetic theory, the most probably speed of a gas particle can computed from:

$$C_{mp} = \sqrt{2R_{sp}T} \tag{2.1}$$

As an example, the most probable speed of molecular nitrogen at room temperature is $\approx$ 422m/s. For porous media flows within TPS materials, bulk flow speeds of $<$ 5m/s are typically encountered. Furthermore, the temperatures can be quite large which will increase the molecular (or thermal) speed. Because the DSMC method is statistical, in the sense that macroscopic quantities are averaged from the individual particle properties, it can be difficult to obtain well-converged statistics. It could be said that there is a "low signal-to-noise ratio."

Because the flows that we are interested in are at very low-speed, we have also had to implement subsonic boundary conditions. As mentioned previously, DSMC has historically and most frequently been applied to high speed flow. In these cases, boundary conditions are imposed simply by supplying high speed particles at the inflow boundary, and deleting them at outflow surfaces. This is both very simple to implement, and physically consistent for hypersonic flows.

For the subsonic inflow we have implemented the boundary condition proposed by Wang and Li[44]. At the upstream boundary, both the inflow pressure, P_{in}, and the inflow temperature, T_{in} must be specified as inputs. The gas number density, n_{in}, is then computed using the ideal gas law.

$$n_{in} = \frac{P_{in}}{kT_{in}} \tag{2.2}$$

Two methods for determining the inflow velocity, u_{in}, were explored. The first is using

a simple zeroth order extrapolation of the interior information, as in:

$$u_{in} = u_j \tag{2.3}$$

The index, j, refers to the value at the first interior cell. The second method invokes the theory of characteristics to compute the inflow velocity based on pressure information from the interior. The equation for the inflow velocity in this case is:

$$u_{in} = u_j + \frac{P_{in} - p_j}{\rho_j a_j} \tag{2.4}$$

Here, a is the local sound speed, and ρ is the local mass density. In both cases, macroscopic values from the interior must be computed based on averages of particles to compute the boundary condition. For example, the instantaneous velocity in a computational cell is calculated as the average of individual particle velocities in the cell, as:

$$u' = \frac{1}{N_p} \sum_{p=1}^{N_p} u_p \tag{2.5}$$

As mentioned previously, subsonic flows pose a challenge due to the large thermal velocities of the indivdual gas particles relative to the bulk speed of the gas. In order to smooth out the fluctuations in the instantaneous sampled velocity, the subrelaxation technique of Sun and Boyd[45] is employed. This essentially uses a weighted average of the instantaneous velocity, with the previous sampled velocity. Thus the averaged velocity at the current timestep is calculated as:

$$\bar{u}^n = \theta u' + (1 - \theta)\bar{u}^{n-1} \tag{2.6}$$

Where $\bar{u}$ is the averaged velocity component, and n is the time level at which it is computed. The instantaneous velocity is given by u'. θ is the subrelaxation factor. There is typically a trade here between smoothness and convergence, with a smaller weighting value for θ resulting in a smoother average velocity, but greater number of timesteps to reach steady-state.

It was found that any differences between solutions produced by the two boundary conditions were not discernible within the fluctuations of the of averaged flowfield – typical "steady-state" solutions still had residual fluctuations in the velocity of $\approx 5\%$. Furthermore, large excursions of the instantaneous velocity during the transient could sometimes lead to unbounded growth in the second inflow condition. Therefore, for the remainder of the analysis, the zeroth order extrapolation approach is employed.

The outflow boundary conditions are prescribed according to the method of characteristics as given by Nance et. al[46]. The outflow pressure, P_{out} is specified. The remainder of the macroscopic properties must be computed using information from the interior of the solution. This is done using:

$$\rho_{out} = \rho_{int} + \frac{P_{out} - p_{int}}{a_{int}^2} \tag{2.7}$$

$$u_{out} = u_{int} + \frac{P_{out} - p_{int}}{\rho_{int} a_{int}} \tag{2.8}$$

$$T_{out} = \frac{P_{out}}{\rho_{out} R_{sp}} \tag{2.9}$$

The implementation within the MGDS code is handled similarly to how one would implement a boundary condition in a computational fluid dynamics (CFD) solver. In a finite volume CFD code, the boundary conditions are typically imposed on so-called ghost cells which lie outside of the computational domain such that when quantities are reconstructed at the domain boundaries, the correct boundary conditions are imposed. Similarly, in the present implementation, computational cells are selected near the boundary such that the correct boundary condition is imposed at a surface within the domain, but sufficiently far from the geometry. This is illustrated in fig. 2.2.

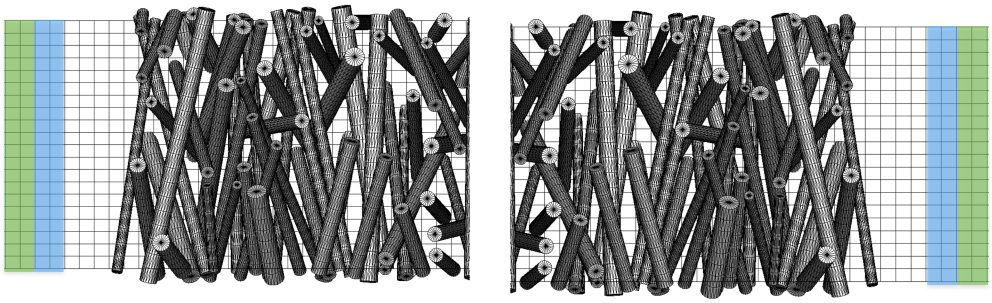

Figure 2.2: Illustration of the implementation of the inflow (*left*) and outflow(*right*) boundary conditions on a cartesian mesh for a typical simualtion of a fibrous microstructure.

In these figures the cells in which the boundary condition is imposed are the green cells. Because of the subsonic character of the flow, information must be obtained from within computational domain in order to compute the proper conditions at the inflow and outflow. This is done by sampling a layer of interior cells shown in this figure in blue. Care must be taken with this type of boundary condition for massively parallel DSMC solvers due to the fact that the current implementation is imposed on a cell-wise basis, which requires information for adjacent cells, and therefore potentially gives rise to inter-processor data dependencies.

2.1.3 Subsonic Validation for Microchannel Flow

Prior to simulating porous media flows, we first wish to verify that we have properly implemented the specialized boundary conditions in each of the codes. To accomplish this, we consider a microchannel flow. We have chosen the same setup as was used in Cai *et. al*[8]. A schematic of the problem setup is presented in Fig. 2.3.

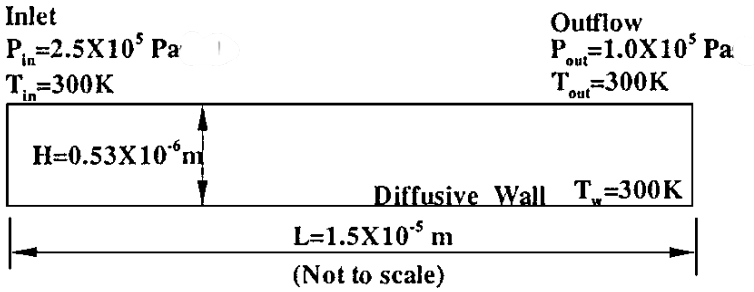

Figure 2.3: Schematic for the microchannel verification numerical experiment[8].

The problem consists of a long narrow channel, with a prescribed pressure gradient which drives the flow from left to right. By simulating this problem we may verify both that the subsonic boundary condition for DSMC has been properly implemented, but also that the slip wall boundary condition for CFD is correct. An analytical solution exists for this problem, and we use the form presented in Cai *et. al*, which is given by:

$$u(x) = \frac{1}{2\mu}\frac{\mathrm{d}p}{\mathrm{d}x}\left(y^2 - \frac{H^2}{4} - H^2 Kn\frac{2-\sigma}{\sigma}\right) \tag{2.10}$$

In this equation, u is the streamwise velocity, $\frac{\mathrm{d}p}{\mathrm{d}x}$ is the streamwise pressure gradient, and y is the spanwise location. The tangential momentum accommodation coefficient (TMAC), σ, has been set to 0.85 for our problem. The TMAC gives the fraction of gas particles which are diffusely (i.e. randomly) reflected from the wall, as opposed to specularly. A TMAC of unity corresponds to a no-slip wall boundary condition.

Fig. 2.4 shows the results of this analysis. In this figure the color contours are from DSMC, the solid lines are from CFD, and the dashed lines are from an analytical solution. Qualitatively, we see good agreement between both methods and the analytical solution. If we look at centerline profiles, as in Fig. 2.5, we also see very good agreement with the computed pressure overlaying the analytical solution. The streamwise velocity profile also gives very good agreement between methods and compared to the analytical solution.

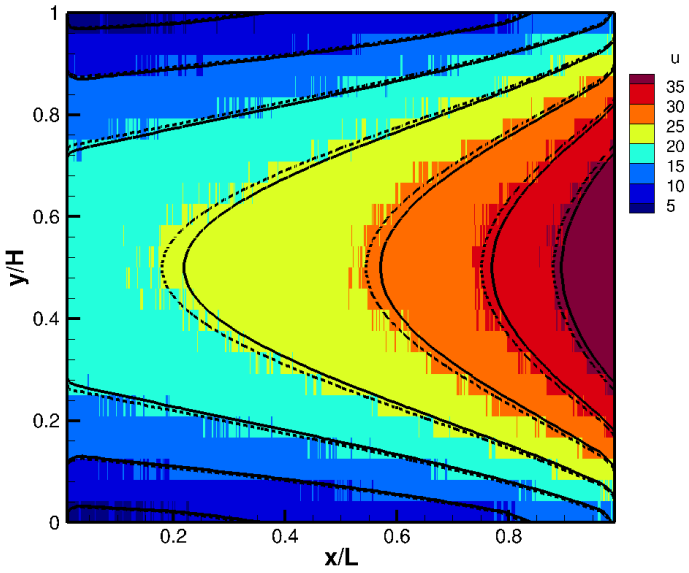

Figure 2.4: Contour plot for the microchannel verification experiment. The lines are from CFD, and the colors are from DSMC. The dashed line represents the analytical solution.

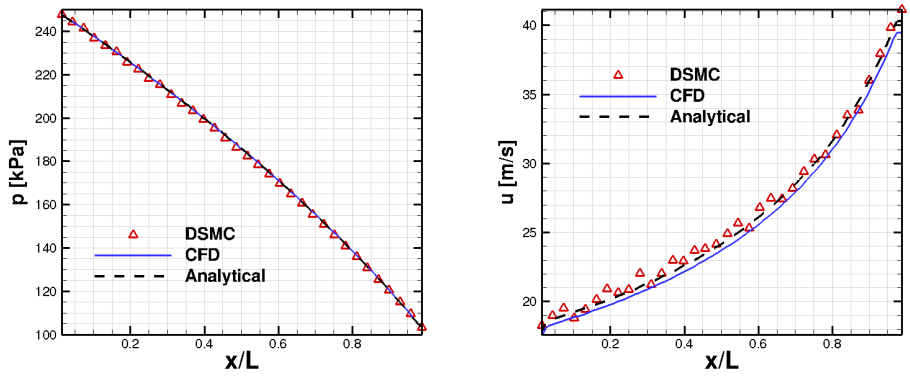

Figure 2.5: Centerline profiles from the microchannel simulations. The left figure shows the pressure, while the right figure shows streamwise velocity.

2.2 Surface Generation

As we are proposing to improve the fidelity of material response modeling by simulating the microstructure of the TPS materials, we must have a framework for generating computational surface meshes which approximate the microstructures. To this end, we have developed a code for generating random arrays of fibers, where we can control the distributions of three-dimensional orientations, fiber diameters, bulk porosity, etc. This code, henceforth referred to as FiberGen, represents the fibrous geometry as an array of straight cylinders. Figure 2.6 shows an example of a surface generated using this code. In this example, we have allowed the fibers to vary about a nominal radius, and orientation. In the right figure, a density profile has been specified in the material to emulate a porous material which has undergone in-depth ablation.

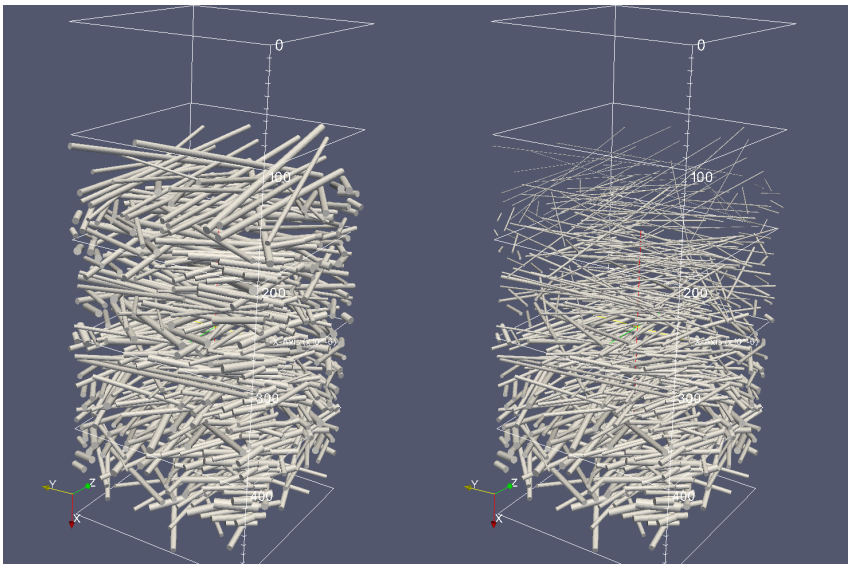

Figure 2.6: Demonstration of the capabilities of the fiber generation code. The geometry on the right has undergone a prescribed "ablation."

The primary user inputs are the dimensions of the domain to be simulated, and the target bulk porosity. Figure 2.7 illustrates the algorithm used to build the geometry in

FiberGen.

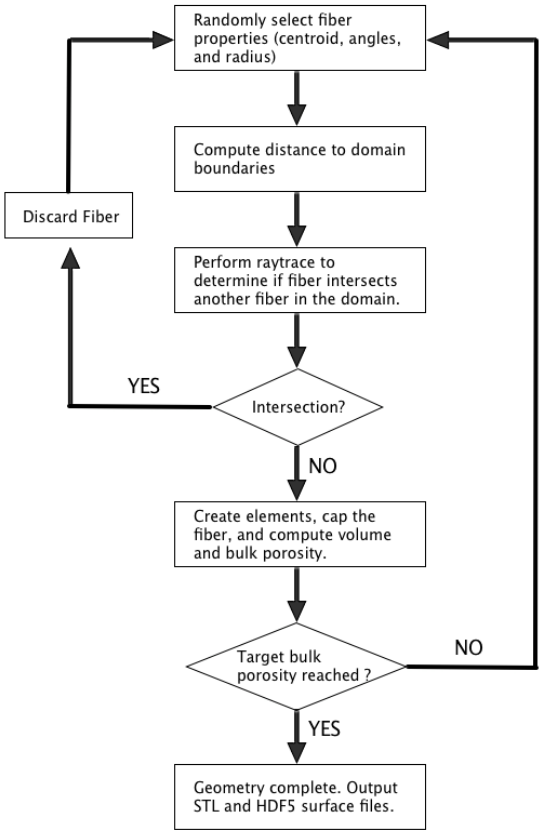

Figure 2.7: Illustration of the FiberGen algorithm in its current implementation.

The fibers created within the code have a hierarchical data structure where each fiber is composed of many elements that subdivide the cylinder along its axis. Each element in turn contains many triangles which are the surface representation used by the DSMC code. An illustration of this hierarchy is presented in Fig. 2.8. Fig. 2.9 shows each of these types for a typical fiber output from FiberGen, with the figure on left highlighting a single fiber, the middle, one of its elements, and the right, one of that element's triangles. These data structures are primarily used in allowing the surface to recess. and will be leveraged to simulate the thermochemical ablation of the fibrous

microstructure.

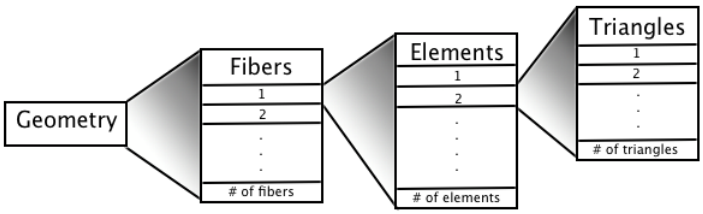

Figure 2.8: Hierarchy of the data structures used in FiberGen.

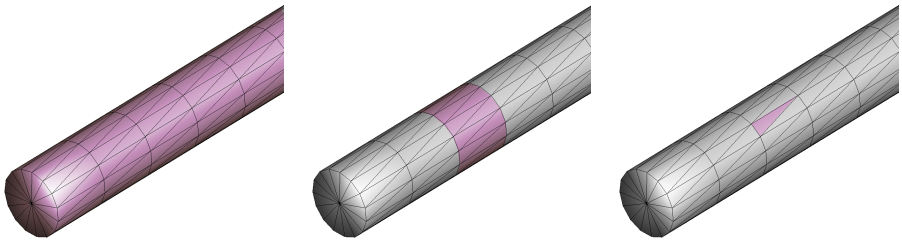

Figure 2.9: Illustration of the hierarchical types for the individual fibers. The figure on the left highlights a "fiber," the middle figure shows an "element," and the figure on the right shows a "triangle."

Algorithm 1 Generate a new random fibrous microstructure

```
1:  procedure GENERATE NEW MESH
2:      {L_x, L_y, L_z} ← user specified doman size
3:      ε_nom ← nominal target porosity
4:      {r_nom, σ_r, θ_max} ← nominal fiber radius, deviation, and maximum elevation angle
5:      while porosity > ε_nom do
6:          generate random properties for a single fiber
7:          compute the axial and radial vectors for the fiber
8:          compute the distance to all of the domain boundaries along axial vector
9:          if (Fiber intersects the inflow/outflow planes within the domain) then
10:             cycle
11:         end if
12:         test to see if fiber intersects another fiber
13:         if (Fiber intersects another fiber within the domain) then
14:             cycle
15:         else
16:             compute rotation matrices for the fiber
17:             create each of the elements for the fiber
18:             pave each element surface with triangles
19:             update the total volume of fibers within the domain
20:         end if
21:         update the bulk porosity
22:     end while
23:     write STL file of surface
24:     write HDF5 file containing fiber and element data
25: end procedure
```

A more detailed description of the FiberGen algorithm as it is implemented within

the code can be seen in Algorithm 1. The user first inputs a domain size to be filled with fibers. This domain must be a rectangular prism having edge dimensions of L_x, L_y, and L_z. Then the user prescribes a target nominal porosity, ϵ_{nom}. The bulk porosity, ϵ, is defined as:

$$\epsilon = 1 - \frac{\textit{Total Volume of Fibers}}{L_x \times L_y \times L_z} \tag{2.11}$$

Therefore, the initial porosity of the microstructure before any fibers have been generated is unity. A typical value for ϵ_{nom} used in this work – and found in TPS microstructures – is 0.90. In addition the user prescribes the nominal fiber radius r_{nom}, the standard deviation of the fiber radius σ_r, and the maximum elevation angle, θ_{max}, with respect to the plane normal to the "pressing" direction.

The code then begins to generate random properties for a test fiber based on these constraints (algorithm step 6). First a random point within the domain is selected to "seed" the fiber, and act as its centroid. The radius of the fiber is assigned by sampling a Gaussian distribution centered at r_{nom} and having a standard deviation of σ_r. Outliers are discarded if the they are greater that 5 standard deviations from the mean. The three-dimensional orientation of the fiber is defined by two angles about its centroid: referred to as the *elevation* and *azimuthal* angles. The elevation angle, θ, is sampled randomly from a uniform distribution with end-point at $\pm\theta_{max}$. The azimuthal angle, ϕ, defines the fiber's rotation about an axis parallel to the pressing direction of the microstucture, and is randomly sampled from a uniform distribution from 0 to 2π radians.

Next, a unit vector aligned with the fiber axis, as well as one pointing radially out from the axis, are computed and stored. These are denoted as $\hat{\mathbf{a}}$ and $\hat{\mathbf{r}}$ for the axial and radial vectors, respectively, and are defined as:

$$\hat{\mathbf{a}} = \begin{bmatrix} \cos\theta \\ \sin\theta\cos\phi \\ \sin\theta\sin\phi \end{bmatrix}, \qquad \hat{\mathbf{r}} = \begin{bmatrix} -\sin\theta \\ \cos\theta\cos\phi \\ \cos\theta\sin\phi \end{bmatrix} \tag{2.12}$$

Then the distances along the fiber axis to each of the six planes that bound the domain are computed using the following relationship from vector calculus:

$$d_i = \frac{(\mathbf{x}_i - \mathbf{x}_c) \cdot \hat{\mathbf{n}}_i}{\hat{\mathbf{a}} \cdot \hat{\mathbf{n}}_i} \tag{2.13}$$

Here, $\mathbf{x}_c$ and $\mathbf{x}_i$ represent the centroid of the fiber, and any point on the target plane, respectively. The subscript i denotes the plane for which the distance along the vector is being evaluated. The two minima of the distances computed are assumed to be planes of intersection within the domain. If the fiber intersects either the inflow or outflow plane, this could allow simulation particles to get inside of the fiber, and thus these fibers are discarded and a new fiber is seeded (algorithm step 6).

The next step is to test whether the new fiber intersects with any existing fibers in the microstructure. This accomplished using a simple ray-tracing algorithm for a cylinder. For any pair of cylinders, this requires their axial unit vectors, their radii, and any point along their axis. These quantities are denoted as $\hat{\mathbf{a}}_i$, r_i, and $\mathbf{x}_i$, respectively. The subscript i indicates the index of the fiber. For illustration purposes we will assume the new fiber that is being tested is subscript 2, and the existing fiber for which we looking for intersection is subscript 1. For the intersection test, the new fiber ($i = 2$) is treated as the *ray*, and the existing fiber ($i = 1$) is the *surface* that may or may not be intersected by the ray. In order to account for the finite radius of the new fiber, its radius is added to that of the existing fiber. In other words we are now testing for intersection of a ray, with a cylinder that has a radius equal to $r_1 + r_2$. For the case of a cylinder, there is an intersection *if* the discriminant $b^2 - 4ac \geq 0$, where:

$$a = (\hat{\mathbf{a}}_2 - (\hat{\mathbf{a}}_1 \cdot \hat{\mathbf{a}}_2) \cdot \hat{\mathbf{a}}_1) \cdot (\hat{\mathbf{a}}_2 - (\hat{\mathbf{a}}_1 \cdot \hat{\mathbf{a}}_2) \cdot \hat{\mathbf{a}}_1) \tag{2.14}$$

$$b = 2(\hat{\mathbf{a}}_2 - (\hat{\mathbf{a}}_1 \cdot \hat{\mathbf{a}}_2) \cdot \hat{\mathbf{a}}_1) \cdot ((\mathbf{x}_2 - \mathbf{x}_1) - (\mathbf{x}_2 - \mathbf{x}_1) \cdot \mathbf{a}_1)) \tag{2.15}$$

$$c = |\mathbf{x}_2 - \mathbf{x}_1 - (\mathbf{x}_2 - \mathbf{x}_1) \cdot \hat{\mathbf{a}}_1)|^2 - (r_1 + r_2)^2 \tag{2.16}$$

If there is an intersection, then the solutions to the quadratic equation $ax^2 + bx + c = 0$ are the two distances along the ray from the centroid to the intersections with the cylinder, as in:

$$\mathbf{x}_{int} = \frac{-b \pm \sqrt{b^2 - 4ac}}{2a} \tag{2.17}$$

Using this, the points of intersection in cartesian space are determined, and if these points lie within the domain, the fiber is discarded, and a new fiber is seeded. If there is no intersection, *or* if the intersection lies outside of the domain, the fiber is accepted.

At this point it is convenient to compute and store a matrix that will be used to translate between the spherical reference frame attached to the fiber, and the cartesian reference frame of the simulation domain. This is referred to as the cross-product matrix and is defined as:

$$\mathbf{K} = \begin{bmatrix} 0 & -a_3 & a_2 \\ a_3 & 0 & -a_1 \\ -a_2 & a_1 & 0 \end{bmatrix} \tag{2.18}$$

This is utilized later on when triangles are generated on the surface of the fiber, where it is necessary to rotate the a point on a radial vector for a fiber about the fiber axis. This is accomplished using Rodrigues' rotation formula, given as:

$$\mathbf{R} = \mathbf{I} + (\sin\theta)\mathbf{K} + (1 - \cos\theta)\mathbf{K}^2 \tag{2.19}$$

The matrix $\mathbf{R}$ is a rotation matrix that can be used to rotate an arbitrary vector about another arbitrary vector, in this case the radial vector for a fiber about its axial vector.

Following this step, the element data structures are built and populated with information about the fiber. All of the individual element radii are set to the fiber radius, r. The length of each element is specified by the user as Δx. Therefore the volume of each element can be computed as:

$$V_{elem} = \pi r^2 \Delta x \tag{2.20}$$

The length of the elements at the end of a fiber (i.e. where it intersects a boundary) are set such that the fiber axis terminates at the boundary. It should be noted that for

fibers that intersect the boundary away from any corners, the volume of the element of intersection within the domain remains as in Eq. 2.20 because the spurious *included* volume is canceled by excess *excluded* volume. For elements whose surface may intersect more than one plane this assumption will likely lead to an error in the volume calculation.

With all element volumes for the new fiber computed, the total volume of the fiber can then be computed as:

$$V_{fib} = \sum V_{elem} \tag{2.21}$$

The porosity is then recomputed including the new fiber, as:

$$\epsilon = 1 - \frac{\sum V_{fib}}{L_x \times L_y \times L_z} \tag{2.22}$$

Once the target porosity has been met ($\epsilon < \epsilon_{nom}$), the code outputs two files for use in the simulations. The first is an STL formatted file containing all of the triangle vertices and face normals. This is the format used by the DSMC solver for surface files. In order to generate all of the triangles for the STL file, using the circumferential grid resolution specified by the user, the rotation matrix given by Eq. 2.19 is used to rotate the radial vector $\hat{\mathbf{r}}$ about the axial vector $\hat{\mathbf{a}}$. for each fiber in the geometry. For example, to place a point on the surface of the fiber at a distance d from its centroid, the following formula is invoked:

$$\mathbf{x}_{surf} = \mathbf{x}_c + d\hat{\mathbf{a}} + r\mathbf{R}\hat{\mathbf{r}} \tag{2.23}$$

Recall that $\mathbf{R} = \mathbf{R}(\theta)$; therefore by varying θ between 0 and 2π, a circle of points is generated on the surface, and the plane formed by those points is perpendicular to the fiber axis.

The second file that is generated is an HDF5 formatted data file containing information for all of the data structures; fibers, elements, and triangles. We employ the HDF5 file when performing simulations where the DSMC flow solver will modify the fibers based on chemical reactions occurring at the surface. The code possesses the capability to read the updated surface information, and reconstruct the surface based on this new data.

Algorithm 2 Update a fibrous microstructure using an HDF5 file

```
1: procedure UPDATE A MESH
2:     read fiber properties from HDF5 file
3:     read update element volumes from HDF5 file
4:     for all fibers do
5:         compute the axial and radial vectors for the fiber
6:         compute the distance to all of the domain boundaries along axial vector
7:         compute rotation matrices for the fiber
8:         construct updated elements
9:         update the total volume of fibers within the domain
10:    end for
11:    update the bulk porosity
12:    write STL file of surface
13:    write HDF5 file containing fiber and element data
14: end procedure
```

Briefly, the algorithm for reconstructing the fiber geometry from the HDF5 file is shown in Algorithm 2. It is not necessary to step through this algorithm in great detail as many of the steps remain the same as those for generating a new geometry. The method for reconstructing the surface for the individual fibers will be explained in greater detail in the following section. The *algorithm* for reconstructing the geometry is in many ways simpler because the tests used to determine fiber validity are no longer required as they have been done when the microstructure was first generated. Thus, rather than randomly generating properties and then testing them, the properties are simply read from the HDF5 file. The main difference is in the construction of the updated elements, which will now be discussed.

2.3 Surface Reconstruction Approach

Performing coupled simulations of an ablating material requires that we have the ability to move the surface as chemical reactions with the gas consume the solid material. The method used to do this should be efficient and robust to handle the complicated geometries under consideration. For this purpose, a simple method is proposed for moving and reconstructing the fibrous microstructures used in the simulations.

Here, the methodology for moving and reconstructing the fiber surfaces is outlined. For this method, the information needed to move and reconstruct the surface is contained within the *element* structure within the hierarchy in Fig. 2.8. An example of a segment of a fiber containing five elements is seen in figure 2.10.

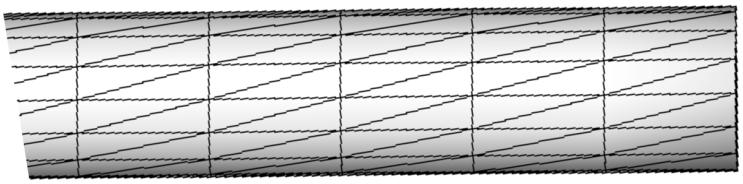

Figure 2.10: Example of a fiber segment containing five elements.

Each element in this segment has a volume as illustrated in Fig. 2.11. Initially, before the simulation is run, the volume of all the elements in a single fiber are equal.

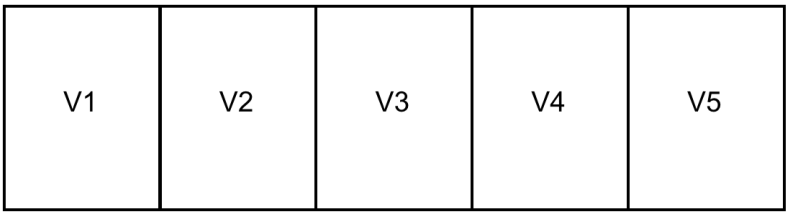

Figure 2.11: Example of a fiber segment containing five elements, each having its own volume.

As the simulation progresses, collisions of simulation particles with triangles belonging to each element can cause reactions which remove atoms from the fiber. This loss of mass is converted to a loss of volume for the parent element. With this new volume the radius of a cylindrical segment having the same volume as the element is computed. This is illustrated in Fig. 2.12.

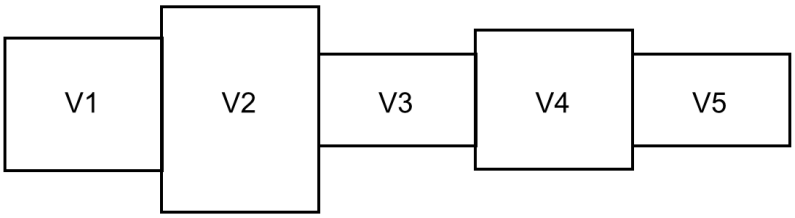

Figure 2.12: Previous example after having undergone some amount of mass loss. The bottom figure illustrates how the new fiber is reconstructed based on the new element volumes.

Each element is then reconstructed as a conical frustum where the two radii are equal to the average of that elements effective radius and its neighbors effective radius. This is illustrated in Fig. 2.13. Here, the five elements seen in Fig. 2.10 have all undergone differing amounts of mass loss.

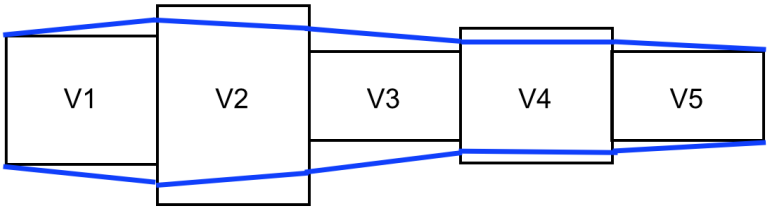

Figure 2.13: Previous example after having undergone some amount of mass loss. The bottom figure illustrates how the new fiber is reconstructed based on the new element volumes.

The final reconstructed shape for this illustration can be seen in Fig. 2.14.

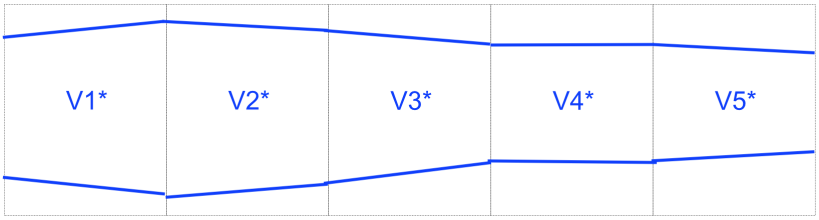

Figure 2.14: Previous example after having undergone some amount of mass loss. The bottom figure illustrates how the new fiber is reconstructed based on the new element volumes.

The volumes in this figures are denoted by a star to indicate that they are not necessarily the same as those in Figs. 2.10 – 2.14. It is important at this stage to note that the *true* volume based on the initial construction and the gas-surface interaction from the simulation is always retained, and is what is operated on during the simulation. In this way, it is insured that mass is conserved, even if there is small error in shape of the surface. Thus the the mechanism whereby the error may manifest itself in the physical solution is in the surface area, and the collision cross-section of the fiber. As will be shown later, the error in the reconstructed volume remains very small throughout. That, in concert with rarefied and stochastic nature of the flow and simulation respectively leads us to assume that the effect of this error on the solution is negligible.

To better visualize how this looks when applied to a complicated microstructure, we present an example seen in Fig. 2.15. Figure 2.16 shows the region highlighted in the red box in Fig. 2.15. The image on the left is of the initial geometry prior to the beginning of the simulation. The image on the right shows the same region after it has undergone some mass loss due to ablation, and been reconstructed according to the algorithm described above. One can see that the fiber in the center of the image has thinned and no longer has a uniform cross-section.

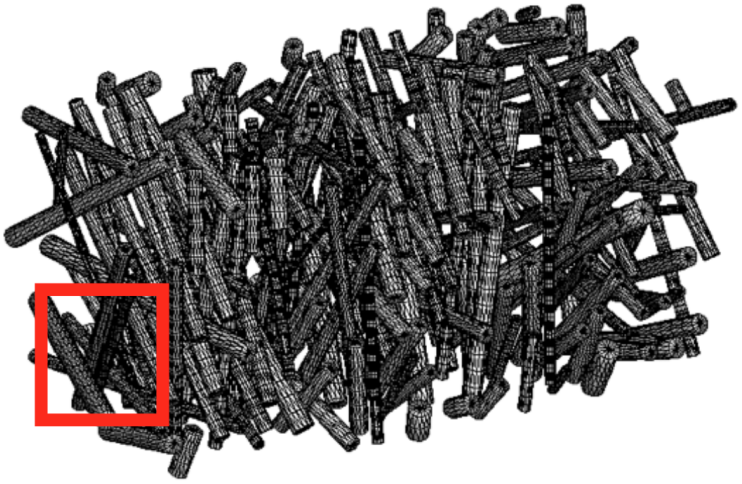

Figure 2.15: Example microstructure which will be used to demonstrate the implementation of the surface motion approach.

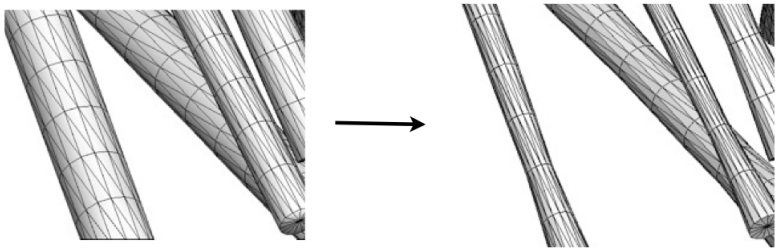

Figure 2.16: Highlighted area from the figure above. The figure on the left shows the virgin microstructure in the highlighted area. The figure on the right shows the same area after it has undergone some loss of mass due to ablation.

It is important to note that one limitation of this approach is that the fibers will always remain axisymmetric, regardless of an asymmetry in the ablative flux at the surface. We know from scanning electron microscope (SEM) images of oxidized carbon preform[10] that ablation at the microscale can be non-uniform, and is often characterized by "pitting" of the surface of the fibers. This type of morphological changes will

not be captured using this method.

Using a method like this *does* have the advantage of being efficient and robust. Determining the shape parameters for each element – namely the two radii – only requires evaluating an algebraic expression. There is no linear system, look-up table, or partial differential equation (PDE) to solve. Additionally, the information required to define the surface is relatively lightweight given that one only is required to store a scalar (the volume) for each element in the microstructure. Furthermore, one is guaranteed to always have a closed surface, and it can handle topological changes by simply removing elements (giving them zero volume).

2.3.1 Assessment of Error in Surface Reconstruction

Since the actual volume of a particular fiber is always known, it is straightforward to directly characterize the error in the volume associated with the reconstruction approach posed in the previous section. Figure 2.17 shows the percent error in the reconstructed volume compared to the "actual" volume for a simulation of the oxidation of a single fiber. The details of this simulation will be discussed in greater detail in Chapter 5. For now, it is sufficient to say that for these simulations the fiber begins as a straight cylinder; as it ablates it takes on a "needled" shape, before being ablated completely.

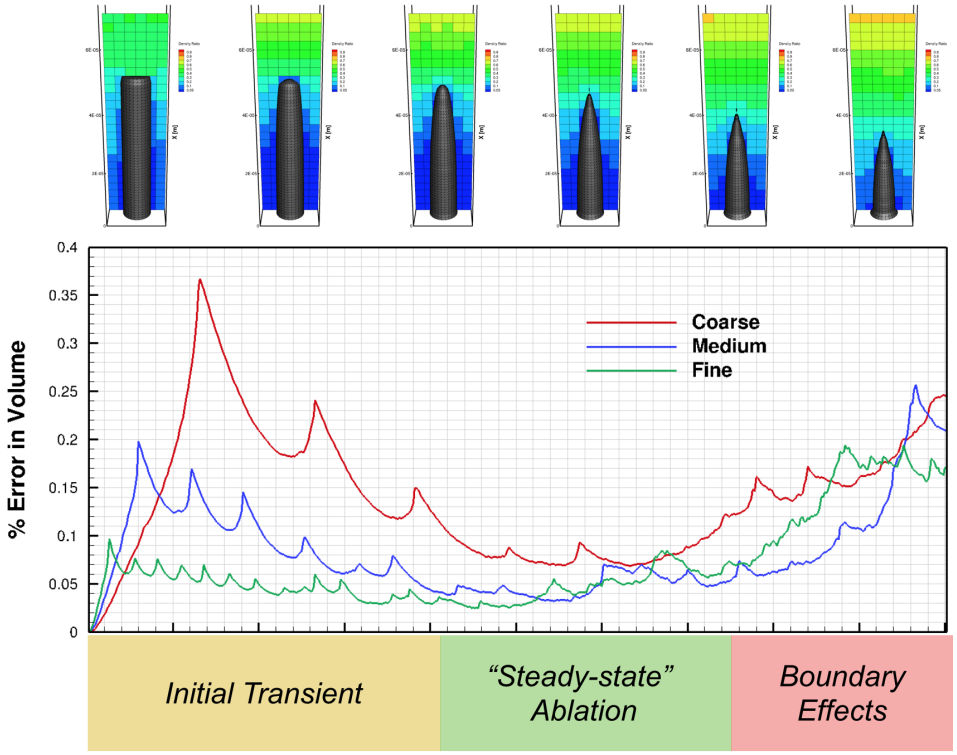

Figure 2.17: % error in the reconstructed volume for a single fiber ablation simulation at three different grid resolutions.

In this figure, the error for three different mesh resolutions has been plotted. As discussed previously, the *actual* volumes of the elements are always retained, so we can then determine the error in the volume of the reconstructed fiber as:

$$\%Error\ in\ Volume = \left| 1 - \frac{\sum^{elements} V_{reconstruction}}{\sum^{elements} V_{actual}} \right| \times 100 \tag{2.24}$$

Based on these analyses three different error regimes are identified. The error tends to be the highest at the beginning of the simulation – labeled here as the "initial transient." This is likely due to highly skewed cylinders that occur near the top of the fiber at the early onset of ablation. After this initial transient, the fiber assumes a pointed configuration which remains self-similar for some time as the ablation proceeds. This is

labeled here as the "steady-state ablation" regime, and has the lowest error associated with it. Finally, as the fiber is nearly completely ablated, the effect of the overlap of the fiber with the domain boundary results again in skewed elements. This results from the interpolation scheme that holds the radius of the element cross-section that lies outside the domain constant, until the element has ablated completely away. Overall, however, the error is quite small and bounded in all cases and all regimes ($< 0.5\%$), and therefore it is concluded that this approach has acceptable accuracy, given its underlying assumptions.

Chapter 3

Permeability of Porous Microstructures

The first aspect of ablative TPS modeling that this methodology is applied to is the transport of gas through the porous medium of the material. As discussed in Chapter 1, the flow of pyrolysis gas through the TPS microstructure is not often modeled in engineering codes. Typically, when it *is* modeled, it is done using simple closures which may not be valid for the flows of interest in ablative TPS modeling. The microscale approach developed in the present work may hold promise in developing and assessing models for pyrolysis gas flow through the porous medium. This chapter will first seek to validate the approach on idealized geometries for which there are empirical relations in the literature, as well as through comparison to computational fluid dynamics (CFD). Then the method will be applied to more realistic microstructures relevant to spacecraft TPS modeling, and compare to existing experimental data.

3.1 Permeability of Square Arrays

3.1.1 Problem set-up

In order to begin to validate the microscale approach which is the subject of the present work to modeling porous media convection, we simulate the flow through simple regular arrays of cylinders. This class of problem has been studied extensively in the literature[47], where one can find many analytical and empirical relations. In addition, due to its simplicity, as well as two-dimensionality, this configuration affords us the opportunity to simulate the flow in the *continuum* regime using DSMC, which would otherwise be prohibitively expensive on complex microstructures. This will demonstrate that we have consistency between different numerical techniques, as well as consistency between this approach and relations in the literature. Typically, these relations attempt to relate the Darcy permeability (Darcy's law, and its variants, are ubiquitous in modeling flow through porous media) of the cylinder matrix to its porosity, which is defined as the ratio of void space to the total volume of the matrix. Later, when attempting to model more realistic materials, we will use a different convention. Here, however, we adopt this convention for the sake of comparison. These relations often use the simplest form of Darcy's law to define the permeability. The form is given by the following:

$$\mathbf{U} = -\frac{\mathbf{K}}{\mu}\nabla p \tag{3.1}$$

Here, $\mathbf{K}$ is the Darcy permeability tensor, μ is the kinematic viscosity of the fluid, and ∇p is the gradient of pressure in the material. $\mathbf{U}$ is referred to in the literature as the superficial velocity vector, and is defined as:

$$\mathbf{U} = \frac{1}{V}\int_{V_f} \mathbf{u}\mathrm{d}v \tag{3.2}$$

Where V is the total volume of the material, V_f is the volume of fluid in the material, $\mathbf{u}$ is the *microscopic* fluid velocity vector in the pores, and $\mathrm{d}v$ is the differential fluid volume element. A consequence of Eq. 3.1 is that the superficial velocity vector is always aligned with the direction of the pressure gradient.

For this analysis, we have chosen the empirical relationship between the permeability and the porosity given by Lee and Yang[9]:

$$\frac{K}{d^2} = \frac{\epsilon^3(\epsilon - 0.2146)}{31(1-\epsilon)^{1/3}} \tag{3.3}$$

This equation gives the permeability, K, normalized by the square of the fiber diameter, as a function of the porosity. We have chosen to adopt this fit, which was derived from finite element calculations, because it is valid nearer to the range of porosities that will be most relevant to our investigation of more realistic materials. By contrast, analytical solutions to this flow in the literature typically require a very high, or very low porosity assumption.

Figure 3.1 shows a schematic of the computational setup for this analysis. It consists of an infinite array of parallel cylinders, having a diameter of 10μm. We vary the porosity from 0.5 to 0.8 by varying the inter-fiber distance. The simulated domain is shown here in red.

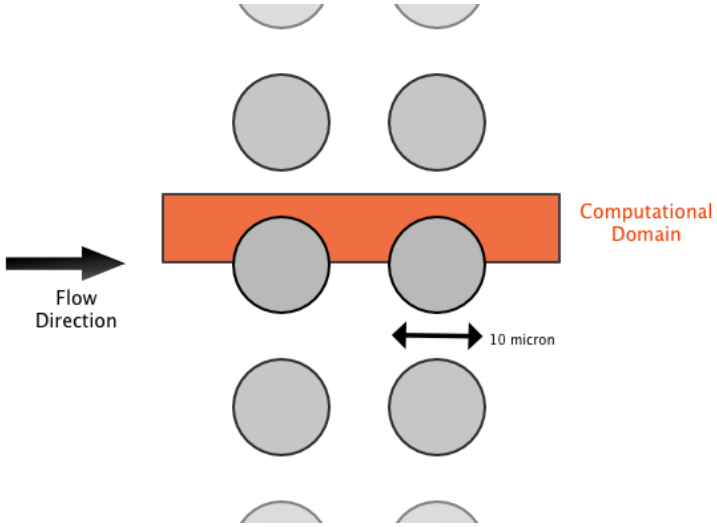

Figure 3.1: Illustration of the computational setup for the simulations on square arrays of cylinders.

At the boundaries, a symmetry boundary condition is applied at the top and bottom

of the domain. In a DSMC code, this means that particles which strike the symmetry surface are reflected specularly. Technically, in both the DSMC simulations and the CFD simulations, the domain is three-dimensional, even though physically the problem is two-dimensional. Therefore, symmetry boundary conditions must be applied on the two boundaries normal to the page in Fig. 3.1. It should be noted that, given that the microstructure for this simple case is periodic, it may be more appropriate to employ a periodic boundary condition at the top and bottom boundaries. However, extending this to non-trivial microstructures – as will be examined in subsequent sections – was deemed prohibitively complex. Thus a symmetry boundary condition is deployed in all cases. Subsonic boundary conditions, as described in Sec. 2.1.2, are applied at both the inflow and the outflow. The interaction with the walls of the cylinder are modeled by a Maxwell slip wall condition[48] in the case of CFD. and by a diffuse wall[37] in the case of DSMC. In both cases, we use a tangential momentum accommodation coefficient (TMAC) of 0.85. The pressure differential across the domain, from left to right, is held constant at 1 kPa. The temperature at the inflow in all cases is 300 K. The inflow and outflow pressures are varied in order to examine the effect of the Knudsen number on the permeability. The matrix of run conditions for this investigation can be seen in Table 3.1. Note that these pressures and temperatures are *not* representative of those experienced by a spacecraft TPS during atmospheric entry. In general, those temperatures would be much higher while the pressures would likely be lower. Both the raising of the temperature and lowering of the pressure produce larger mean free paths, making them more amenable to simulation with the DSMC. The simulations shown in this section are either continuum or very near to it, and are only made tractable for simulation using DSMC by the two-dimensionality of the problem.

ϵ	Δp [kPa]	P_{inf}[kPa]	P_{out}[kPa]	T [K]	Kn
0.50, 0.65, 0.80	0.1	6.65	6.55	300	1.00
.	.	66.5	66.4	.	0.10
.	.	133.1	133.0	.	0.05

Table 3.1: Test matrix for the square array calculations.

3.1.2 Results for square array

Figure 3.2 shows contours of u velocity for a typical simulation of this problem. The top half of the figure shows contours from DSMC, and the bottom is from CFD. The Knudsen number for this simulation was 0.005 based on the fiber diameter, putting it in the slip-flow portion of the continuum regime. The grid cells seen in the DSMC simulation are sized to match the mean free path of the gas. Qualitatively, we see good agreement between the two methods in a regime for which they should both be valid.

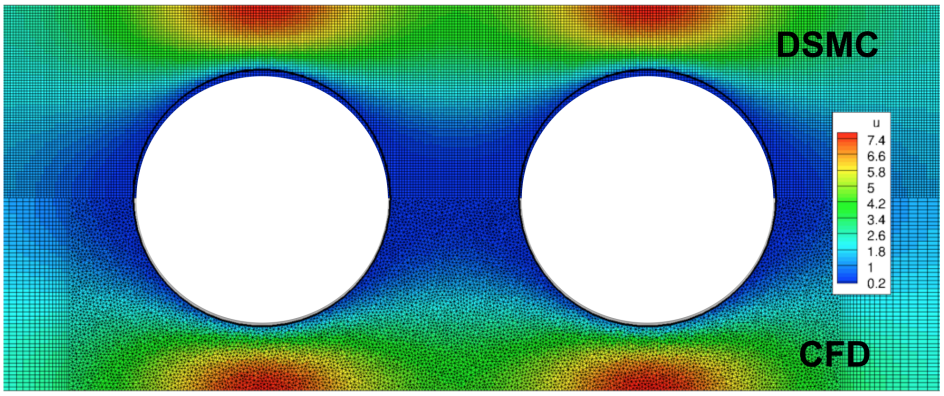

Figure 3.2: Contours of u velocity for the square cylinder array configuration for both DSMC (*top*), and CFD (*bottom*).

Figure 3.3 shows the results from the analysis of the square array configuration at

several porosities, as well as Knudsen numbers. The plot shows the Darcy permeability normalized by the square of the fiber diameter, K/d^2, for porosities ranging from 0.5 to 0.8. We also plot results for various Knudsen numbers to examine the impact of rarefied gas effects on the permeability.

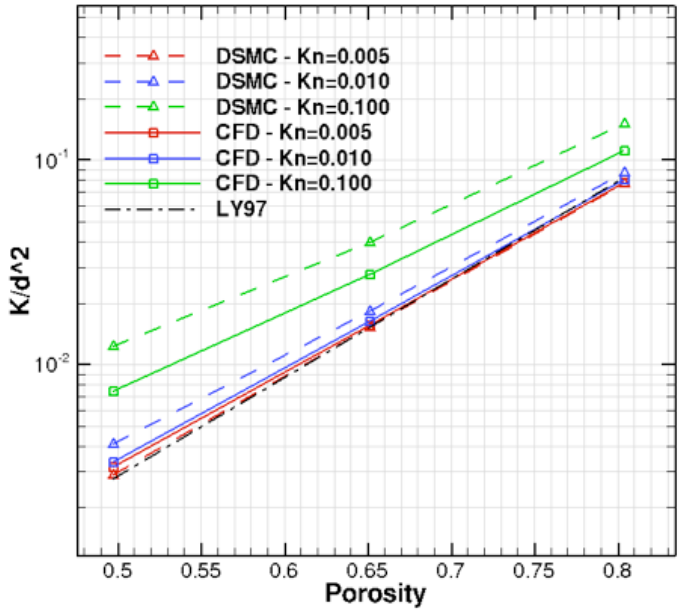

Figure 3.3: Normalized permeability versus porosity for various Knudsen numbers, from both DSMC and CFD. The empirical relation from Lee and Yang[9] is shown by the dash-dot line.

The results from these simulations, both CFD and DSMC, show very good agreement with the empirical model from Lee and Yang[9] for continuum and velocity-slip regime Knudsen numbers. For a Knudsen number of 0.1, which lies firmly in the transitional regime, we observe divergence from the model, as well as divergence of the two numerical methods from each other. This indicates that rarefied flow effects tend to increase the permeability of a material. This is consistent with intuition as slip near the wall results in reduced losses due to shear stress.

3.1.3 Results for random array

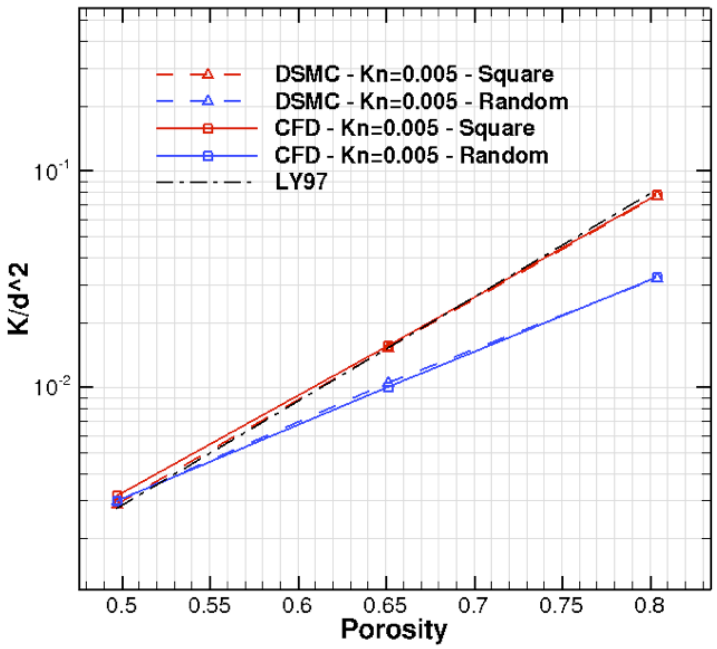

Figure 3.4: Plot showing the permeability of a random array of two-dimensional cylinders compared with the square array.

Finally, in Fig. 3.4 we begin to examine the effect of microstructure on permeability for the case of two-dimensional cylinder arrays. Here, we compare CFD and DSMC simulations of the square array to randomly placed cylinder arrays that have the same porosity. It is difficult to discern between the DSMC and CFD lines in this plot as they lie nearly on top of one another. For these cases, we have used continuum Knudsen number conditions. From this plot we can see that, for these cases, using a random array of cylinders decreases the permeability of the matrix. This is to be expected as the path that the typical fluid element must take through the matrix becomes more tortuous when the complexity of the arrangement is increased from the simplest case.

3.2 Permeability of Carbon Preform

Having demonstrated agreement between this approach and a literature model for a highly idealized porous medium, we now turn our attention to more complex microstructures. Here, we will use the FiberGen tool described in chapter 2 to generate fibrous microstructures which better approximate those found in spacecraft TPS materials. In particular, we would like to apply the computational approach to estimating the permeability of the FiberForm®. This material is used as the preform in the Phenolic Impregnated Carbon Ablator (PICA)[4],[49] material used on many entry vehicles today. It consists of carbon fibers with diameters of ≈ 5 to 6μm. Fig. 3.5 shows a scanning electron micrograph (SEM) of FiberForm® from Panerai, *et al.*[10]. One thing to note from this image is that – although the fibers themselves are $\approx 5-6\mu$m in diameter – in processing they tend to stick together to form bundles which have a larger effective diameter. This will become important in later comparison.

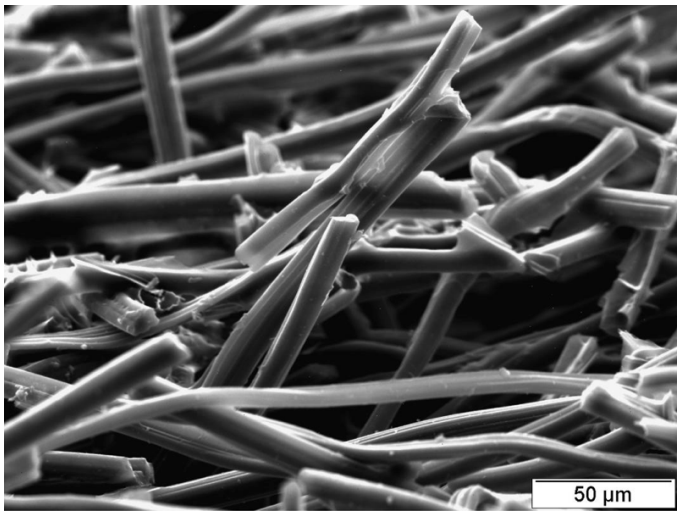

Figure 3.5: Scanning electron micrograph (SEM) of a FiberForm® sample [10].

Marschall and Milos[11] performed permeability experiments on FiberForm® using a flow-tube apparatus. These experiments involved forcing air flow through a cylindrical

plug of the material, and measuring the pressure upstream and downstream of the sample. A diagram of the experimental apparatus from their paper is seen in Fig. 3.6.

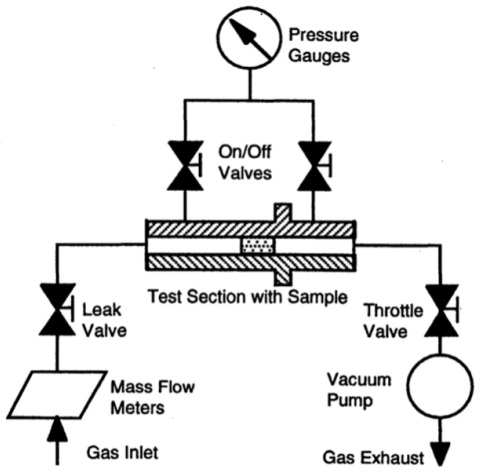

Figure 3.6: Diagram of the experimental apparatus used in the FiberForm permeability experiments [11].

For the analysis in the paper they used the following form of Darcy's law:

$$\dot{m} = -\frac{\pi A M}{\mu R T} K P \frac{\mathrm{d}P}{\mathrm{d}x} \tag{3.4}$$

Where A is the cross-sectional area of the sample, M is the molar mass of the gas, R is the universal gas constant, T is the temperature of the gas, and P is the pressure. The permeability K in their analysis takes the Klinkenberg form, and is defined as:

$$K = K_0(1 + b/P) \tag{3.5}$$

This form contains an additional parameter from the standard form - the constant b. This additional term, they assert in their paper, represents the relative importance of rarefied gas effects on the permeability, whereas the standard Darcy permeability, K_0, is determined primarily by the microstructure geometry. In their data reduction, they

define a permeability constant F given by:

$$F = \frac{\mu \dot{m} T L}{A M \Delta P} = K_0(P_{av} + b) \tag{3.6}$$

With P_{av} being the average pressure across the sample, and ΔP being the pressure difference across the sample. In their analysis, they found exceptionally good fit between this relation and their data, and we adopt this convention for the remainder of this analysis.

For the current analysis, many random fiber geometries were generated. Both the nominal fiber radius and the the nominal fiber elevation angle have been varied in order to examine the sensitivity to these parameters. For all cases presented, the nominal porosity was held constant at 0.9. Subsonic inflow and outflow conditions were prescribed (as described in Sec. 2.1.2) such that the pressure difference was held nominally to $\approx$ 100 Pa. Average pressures ranged from 300 to 2000 Pa. At the spanwise boundaries, we have imposed symmetry conditions. It should be noted that periodic conditions would be more consistent with the assumptions for this problem, however the difficulty of creating a truly periodic microstructure was considered prohibitively complex for the current work. Instead, we will attempt to mitigate any inaccuracy caused by this assumption by selecting a domain size which minimizes this effect. Figure 3.7 shows a typical domain and microstructure from the simulations in the remainder of this chapter.

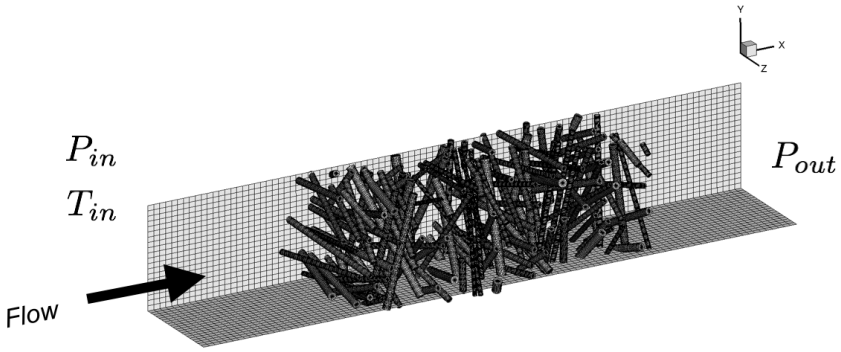

Figure 3.7: Illustration of the set-up for the FiberForm permeability simulations.

It would not be tractable to simulate a geometry with the same dimension as the experiment. This should not be necessary, as the materials should be fairly homogeneous. However, it is important to ensure that a large enough volume to constitute a valid representative volume element (RVE) is simulated. Therefore, three different domain sizes having spanwise dimensions of 50, 75, and 100 μm have been simulated. For these cases, a nominal average pressure of 450 Pa has been used. Fig. 3.8 shows flowfield visualizations for the three different domain sizes.

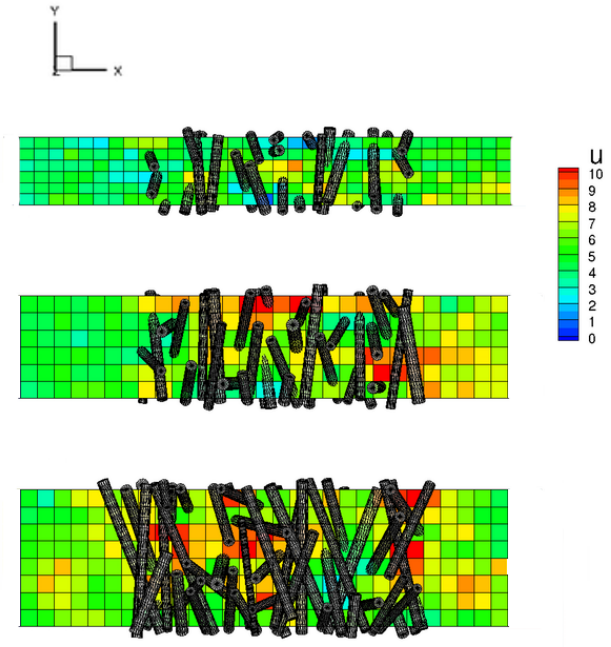

Figure 3.8: Flow visualizations for the flow through FiberForm®-like material for spanwise domain sizes 50μm (*top*), 75μm (*middle*), and 100μm (*bottom*). Pressure difference is $\approx$ 100Pa. Contours are of u-velocity with units of m/s.

The size of the domain should be such that it does not affect the permeability. In order to account for variability in the randomly generated geometries, four separate geometries at each domain size have been simulated. Fig. 3.9 shows the effect of the domain size on the permeability parameter F. The shaded area in this plot represents the standard deviation, and the line approximates the mean of the permeability. It is observed here that increasing the domain size tends to increase the permeability. Further investigation is required to fully determine the reason for this, but it is likely due to the flow "finding" larger pores in the larger domain size. It can be seen in Fig. 3.8 that the larger pores have higher flow velocities, possibly resulting in higher mass fluxes through the bulk. Additionally, there seems to be less scatter for larger volumes. This is easily

explained as the smaller domain will be much more sensitive to random variability in the size and orientation of the individual fibers.

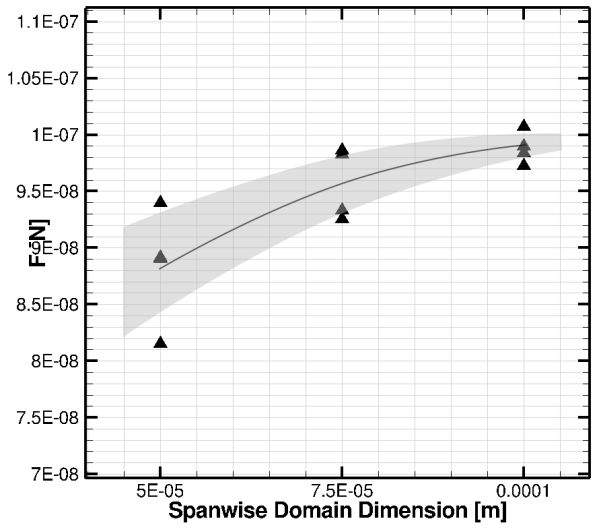

Figure 3.9: Effect of domain size on permeability for P_{avg} of about 450Pa. The shaded area approximates the standard deviation envelope of the different runs at each size.

As can be seen in Fig. 3.5, the actual microstructure of FiberForm® is too complex to be readily defined by a few parameters. For example, it is apparent that, in reality, the fibers tend to group together into bundles. Therefore, perhaps one should use the average bundle diameter instead of the fiber diameter when generating analog surfaces. Furthermore, it is known that FiberForm® is orthotropic due to the manufacturing process where the fibers are pressed into billets. Due to this pressing, fibers have a bias toward being oriented perpendicular to the pressing plane.

In FiberGen, one can prescribe a range of fiber angles relative to the pressing plane. In order to assess the sensitivity of the permeability to this parameter, many different random microstructures with fiber angle ranges of 15 and 25 degrees have been simulated. Simultaneously, for these simulations, the nominal fiber diameter as well as the

average pressure are also varied. Fig. 3.10 shows the permeability for several cases having average pressures ranging from 300 Pa to 2000 Pa. In this plot, a weak sensitivity to the fiber angle over this range is observed, with the tendency being for increasing fiber angle relative to the plane perpendicular to the flow to *increase* the permeability over this range of angles. This relationship is consistent with intuition as the projected area of the fibers onto the pressing plane (perpendicular to the flow) is smaller as the angle of the fibers relative to this plane is increased. In other words, as the fibers become more aligned with the flow, the drag is decreased. The large amount of scatter observed in this plot indicates that the sensitivity to the other parameters varied in these simulation is greater than that to the fiber angle.

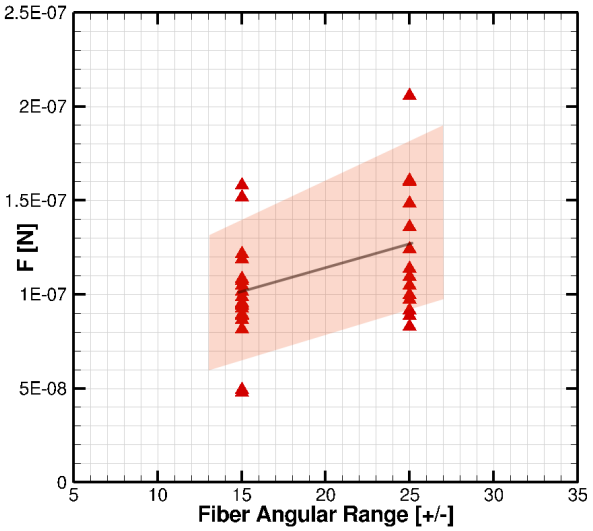

Figure 3.10: Effect of range of fiber orientations on permeability for P_{avg} across all pressures.

Ultimately, we wish to compare the results of these simulations to the data presented in Marschall and Milos[11]. Fig. 3.11 shows the results of our simulations for three different combinations of fiber radius and angle relative to the pressing plane, compared

to the four curve fits presented in Marschall, *et al.*. For the experiments, they ran four different samples in order to account for manufacturing variability in the material.

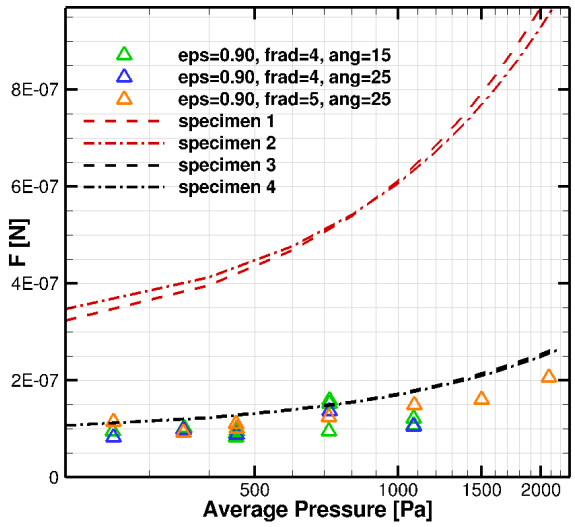

Figure 3.11: Plot showing results from simulations compared to the curve fits from the experiments of Marschall and Milos[11].

As can be seen in this plot, there is a significant variability between the first two specimens and the second two. There is no explanation for this difference, beyond quality control in the FiberForm® manufacturing process in the 1990's when these experiments were carried out. Due to the scatter in these curves, it is difficult to form definitive conclusions about the results presented here. However, we do observe that the results of the computations agree much better with the second two experimental runs, both in magnitude and trend. Furthermore, it is difficult to draw conclusions regarding the sensitivity to fiber radius from this plot. However, if we look at the two fiber radii simulated in isolation, as in Fig. 3.12, we can see that the larger fiber radius shows overall better agreement with experiment, perhaps suggesting that it is more appropriate to base the effective diameter on that of a fiber *bundle* rather than that of

an individual fiber.

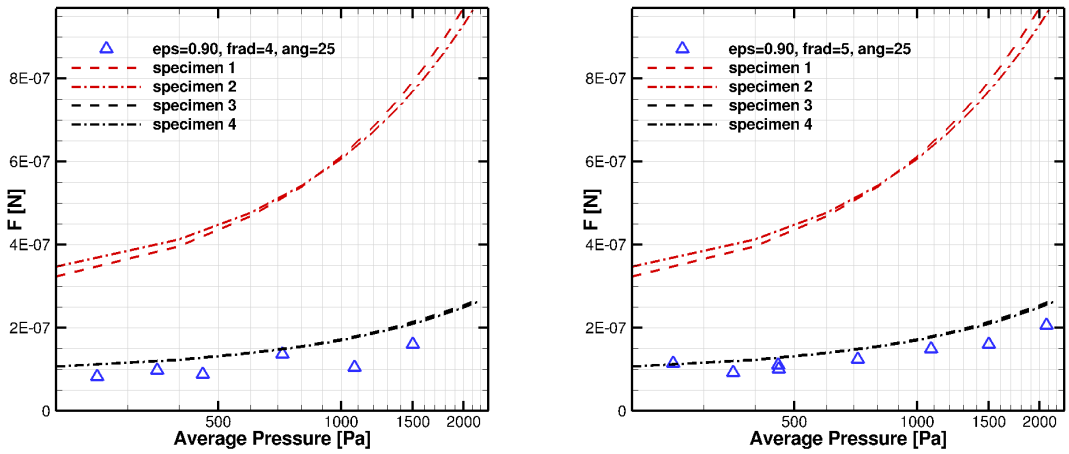

Figure 3.12: Plots showing computed permeability compared to experiment for two nominal fiber radii: 4 μm (*left*) and 5 μm (*right*).

Chapter 4

Ablating Microstructures

In this chapter, simulations are presented which leverage the mesh surface motion technique developed in chapter 2 in order to allow the material to recede under the influence of thermochemical ablation. The feasibility of using this approach at realistic conditions is assessed. Additionally simulations are performed on fibrous microstructures that provide insight into the phenomenon of oxidation within porous media.

4.1 Single Fiber Studies

This section details the algorithm for coupling the previously detailed surface representation and reconstruction approach to the DSMC solver, and calculations are performed on single fibers using reaction rates from the literature.

4.1.1 Coupling Approach

Using the algorithm for moving the surface detailed in chapter 2, we can now perform simulations where the motion of the fiber surface is coupled to the gas-phase solution computed from DSMC.

Briefly, the algorithm for performing a coupled simulation is as follows. First a "virgin" microstructure is generated with user prescribed characteristics using the FiberGen

code detailed in chapter 2. The surface is then cut out of the three-level Cartesian mesh generated by MGDS, and the solver is run for some time. During the simulation, the number of surface atoms that are removed due to gas-surface reactions are tracked. Once there has been significant amount of material lost due to ablation, or at a user specified interval, the surface is updated using the method described in the preceding section. The updated surface is cut out of the cartesian mesh, and the simulation continues. A diagram of the simulation algorithm is shown in Fig. 4.1.

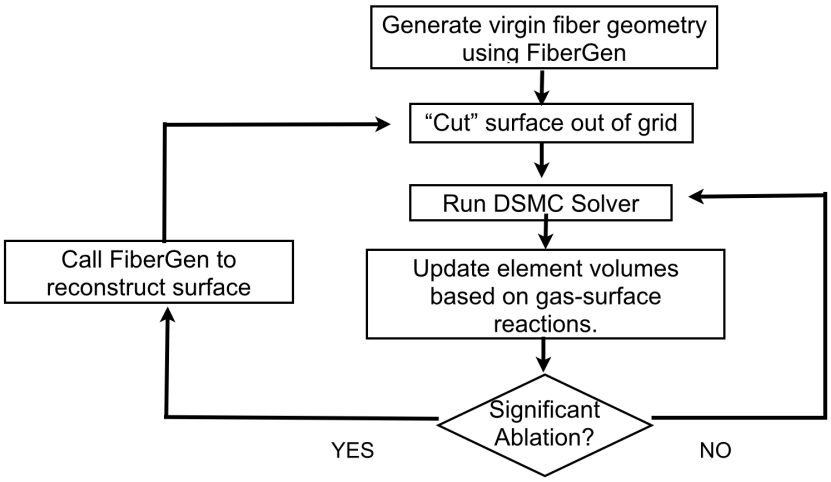

Figure 4.1: Illustration of the algorithm used for performing coupled simulations.

In the case of the simulations presented in the current study, the surface is updated after a specified number of time steps, referred to as the coupling interval. In a subsequent section the effect of the choice of coupling interval will be examined. Figure 4.2 shows example visualizations of a simulation which uses this coupled approach. In this case, there is single carbon fiber which is undergoing diffusion limited oxidation. This test problem will be examined in greater detail in subsequent sections.

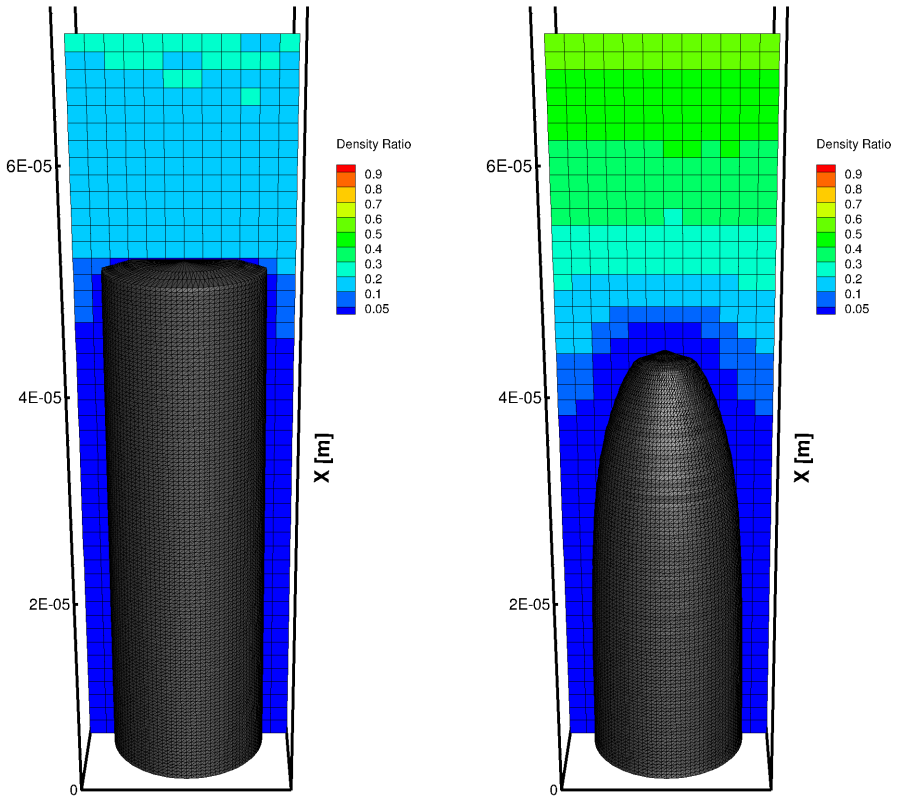

Figure 4.2: Example visualizations of a single carbon fiber undergoing diffusion limited oxidation.

4.1.2 Gas-Surface Interaction Modeling

In DSMC, the implementation of gas-surface interaction models is relatively straightforward. That is it involves determining what to do when a simulation particle strikes a surface, in our case a triangle. In the case where there is no gas-surface chemistry, a diffuse reflection approach is typically imposed[37]. In the case of a fully diffuse surface boundary condition, the particle bounces off the surface in a random direction with a velocity sampled from a Maxwell-Boltzmann distribution centered about the temperature of the wall. We say then that the particle, after it has been reflected, is thermally

accommodated to the wall.

For treating chemical reactions at a surface, the simplest gas-surface chemistry model then involves determining the probability that when a particle strikes the surface, it will react with the surface. In principal, one can apply an arbitrary level of sophistication to determining this probability. Currently, this is an active area of research with researchers investigating methods for using molecular dynamics (MD) simulations to derive reaction probabilities based on the incident energy *and* angle of the particle [50]. The methodology presented in this work is developed in such a way that it can use inputs from these state-of-the-art approaches as they become available.

For the present study, two oxidation pathways are investigated separately. The first is the oxidation of carbon by molecular oxygen given by the following chemical equation:

$$O_2 + C(s) \rightarrow CO_2 \tag{4.1}$$

The second is the oxidation of carbon by atomic oxygen as in the following chemical equation:

$$O + C(s) \rightarrow CO \tag{4.2}$$

Illustrations of these two mechanisms cant be seen in figure 4.3, which shows an incident reactant particle striking a simulation surface triangle to produce either CO or CO_2.

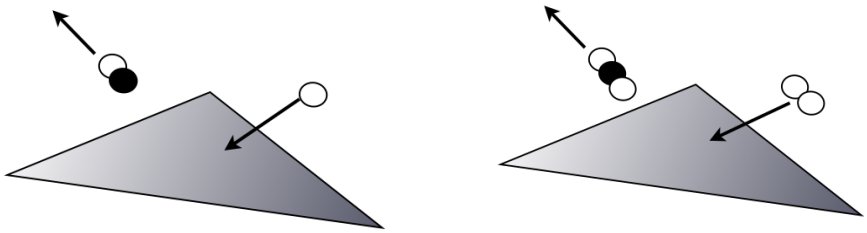

Figure 4.3: Illustration of the two heterogeneous reactions used in this work. The left figure depicts the oxidation of carbon by atomic oxygen, and the right is by molecular oxygen.

In hypervelocity flows such as those found in spacecraft entry applications, atomic oxygen can often be found in abundance in the shock layer, as well as the boundary layer, therefore this is an important mechanism in understanding the ablation of TPS materials. The reaction probabilities provided by Park[12], [13] are used in the following simulations. They are provided in the papers as functions of the wall temperature, T_w. For the oxidation of carbon by molecular oxygen the probability is given as:

$$\alpha = \frac{1.43 \times 10^{-3} + 0.01 \exp(-1450/T_w)}{1 + 2.0 \times 10^{-4} \exp(13,000/T_w)} \tag{4.3}$$

And for atomic oxygen, the probability used is:

$$\alpha = 0.63 \exp(-1160/T_w) \tag{4.4}$$

It is important to note a couple of things about these probabilities before we continue. The first is that the probability for the atomic oxygen pathway is technically given as the probability of *adsorption* of atomic oxygen to form surface CO. This reaction will still consume gas-phase oxygen as well as surface carbon in the same proportions, however in the present study we do not model the subsequent *desorption* of CO from the surface, but rather release the CO molecule instantaneously. The second thing to

note is that the probabilities provided by Park are derived from experiments performed on graphite at the macroscale. Therefore the probabilities can be interpreted to account for both the atomistic chemistry at the surface, but also the effect of *micro*scopic surface roughness. For example, if the surface of the experimental specimen was rough, this could be expected to augment the probability of surface reaction above what one would expect from purely chemical considerations. However, the aim of this work to assess the *feasibility* of performing these simulations with the best available models; seeking higher fidelity gas-surface models is an active area of research, but is beyond the scope of the current study.

To better understand the relative magnitude and behavior of these two equations, they are have been plotted over the range of temperatures relevant to this study in figure 4.4. The dashed-dot lines in this figure show the two temperatures that will be investigated in the following section. The dashed line in this figure shows approximately the temperature at which sublimation - that is the direct phase change of solid carbon to gas - becomes the dominant ablation mechanism at the pressures under consideration here. The most important thing to note about this figure is the relative magnitudes of the two probabilities. There is a roughly two order of magnitude increase for the probability of oxidation by atomic oxygen versus molecular oxygen.

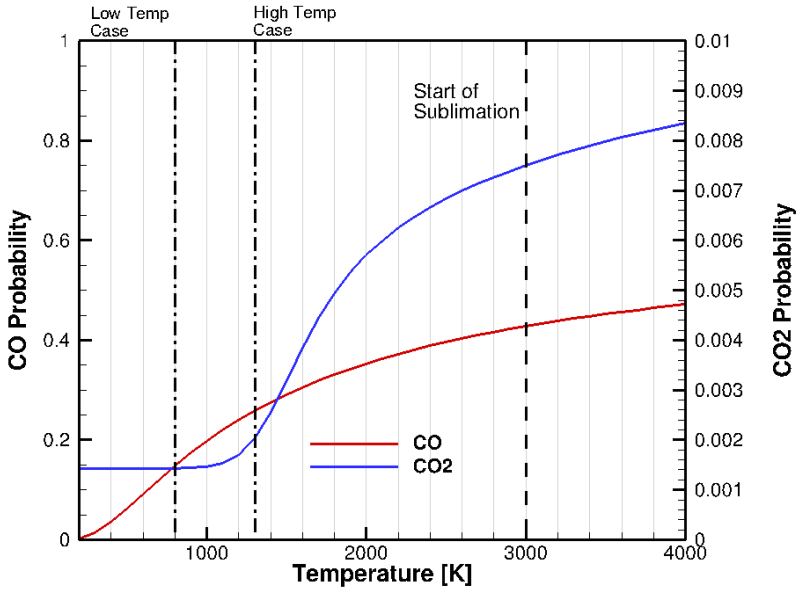

Figure 4.4: Reaction probabilities from Park [12],[13] as a function of temperature. The location of the 800K case and the 1300K case are shown by the dash-dot lines. The dashed line illustrates the approximate temperature at which sublimation becomes important at these conditions.

To gain further intuition about the thermochemistry of the carbon-oxygen system, an equilibrium calculation was performed using the Gibbs free energy minimization procedure used by the Chemical Equilibrium with Applications (CEA)[51] code. The results of this are shown in figure 4.5. The output of this calculation gives us relative molar concentrations of each of the prescribed species for a given temperature and pressure. In this case, the species that were input were O, O_2, CO, and CO_2, as well as two gaseous carbon species, C and C_2. It should be noted that C_3 is another predominant species at high temperatures. This species was omitted from this calculation, but as our primary interest in this work is oxidation at temperature well below the sublimation temperature of carbon, its omission is not likely to effect the results.

Again, in this figure, the two temperatures that will be investigated in the following

section are shown by dashed-dot lines. It is clear from this plot that there is a temperature at which the dominant product species in the gas phases transitions from being CO to CO_2. This temperature corresponds roughly with the equilibrium temperature of the so-called Boudouard reaction [52], which serves to regulate the the relative amount of CO/CO_2 in the gas-phase. This temperature also plays an important role in the design of experiments [53] which may be used in future work for validation of the modeling approach in this work. It is also interesting to note that, in this diagram, there is no oxygen (molecular or atomic) present at any temperature. The implication of this is that if one were to expose a piece of graphite to air, it would spontaneously change to CO_2. While this is true, this diagram does not tell you that the rate of this process is *very* slow.

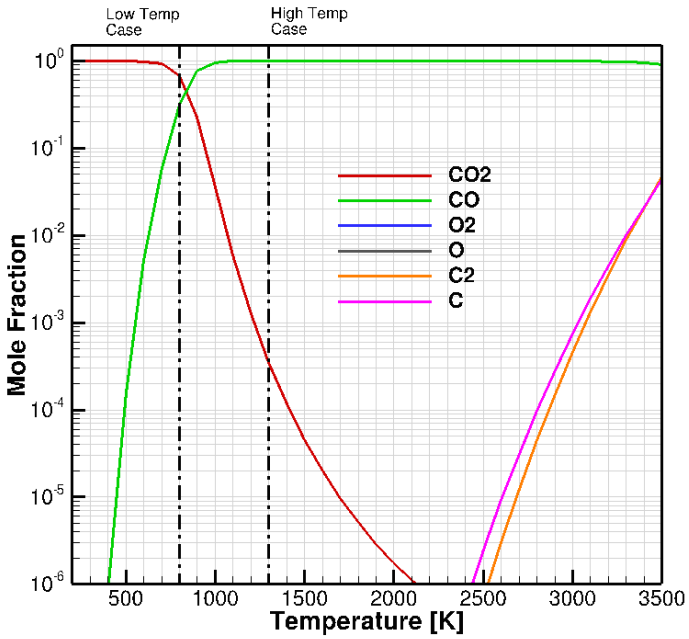

Figure 4.5: Equilibrium mole fractions for the carbon-oxygen system as a function of temperature. Note that this is for $p = 0.040$atm. There is minimal difference between this condition and $p = 0.067$atm.

In order to couple this gas-surface interaction model to the treatment of the microstructure surface detailed in chapter 2, we simply need to keep track of how many atoms of surface material are lost for each element due to either Eq. 4.1 or 4.2 at the surface of its constituent triangles. Note that in the DSMC method, each simulation particle typically represents a very large number of actual particles. For example, in a typical simulation from the subsequent section, a reacting surface collision will remove approximately one million atoms of carbon from the surface.

4.1.3 Problem Setup

To demonstrate the coupling methodology and gas surface interaction model described in the previous sections, a simple test case is proposed. In this case, a single carbon fiber is exposed to oxygen (either atomic or molecular) diffusing onto it from above. An illustration of the simulation set-up is seen in figure 4.6.

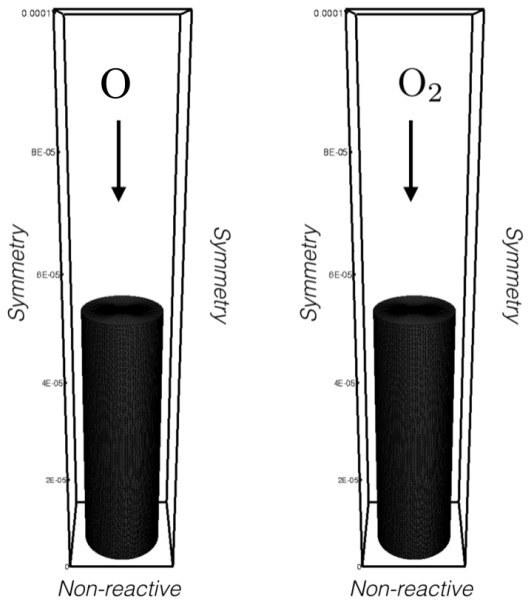

Figure 4.6: Diagram showing the problem set-up for the single fiber test cases. The left figure represents test cases 2 and 4, while the right figure is for test cases 1 and 3.

For the results presented in this section, the diameter of the fiber is 10μm, and the dimensions of the domain are $20\mu\text{m} \times 20\mu\text{m} \times 100\mu\text{m}$. Neglecting the empty top half of the domain, this corresponds to a porosity of approximately 0.80. (Note that Fig. 4.6 is for illustration purposes; the fiber seen in the figure is larger that that simulated subsequently). The gas surface interaction is governed by either of the two reactions provided in the previous section (Eqs. 4.1 and 4.2), depending on which reactant is provided at the top boundary. Simulations have been run at two different temperatures: 800K and 1300K. Based on Fig. 4.5 it observed that these two conditions lie on either side of the Boudouard equilibrium temperature. At the lower temperature it is expected that the O_2 – CO_2 system is more representative. Similarly, at the higher temperature it is expected that the O – CO system is likely more representative. The matrix of test conditions that were simulated and whose results are presented in this section is shown in Table 4.1.

Case	Reactant	Product	T_w [K]	α
1	O_2	CO_2	800	0.00143
2	O	CO	800	0.14778
3	O_2	CO_2	1300	0.00204
4	O	CO	1300	0.25800

Table 4.1: Test matrix for the coupled single fiber simulations.

The reaction probability, α, shown in Table 4.1 is computed using either Eq. 4.1.2 or Eq. 4.1.2 depending on the reactant used. Note that α is a constant. For these simulations the wall is not heated nor cooled by gas-surface interaction, thus the wall temperature T_w is a constant. Simulating the heat transfer due to surface chemistry through the solid is an area of future work.

4.1.4 Results

This section presents results from the simulations run at the conditions shown in Table 4.1. Those results are used to examine the effect of the choice of coupling frequency, as well as the reaction pathway on the performance and prediction of the method.

Effect of coupling frequency

The first thing that is of interest to investigate using this simple test problem is the effect of the choice of the coupling interval on the results of the simulation. Because of the disparity between the molecular timescale of the gas which dictates the size of the timestep taken in the DSMC method, and the timescale of the shape change of the solid caused by ablation we certainly do not need to update the shape of the solid at every timestep. The question remains however, what *is* an appropriate choice of this parameter, and what is the impact of the surface reconstruction on the computational cost of the simulation?

Figure 4.7 shows the effect of the coupling frequency (1/coupling interval) on the cost per iteration (or timestep) in wall clock for a simulation at condition 4 from Table 4.1. From this plot it can be seen that below a certain frequency the surface update appears to add very minimal cost to the overall simulation.

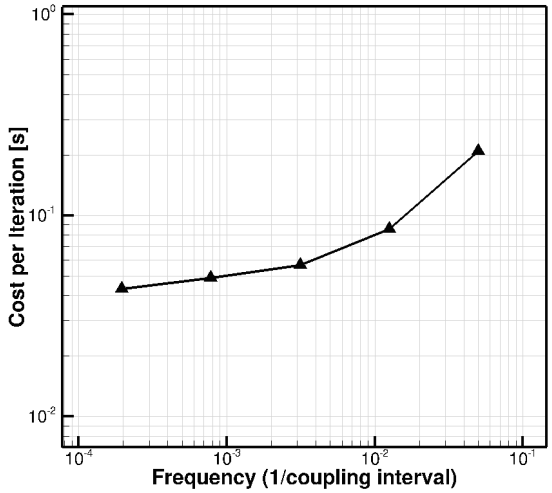

Figure 4.7: Effect of coupling frequency on the wall clock time of the simulation.

Another important effect to attempt to quantify is the effect of the coupling interval on the predicited microstructure morphologies. Figure 4.8 shows the predicted fiber radius for various choices of coupling interval. It can be seen that for this range of coupling intervals there is effectively no impact on the shape of the fiber at this time.

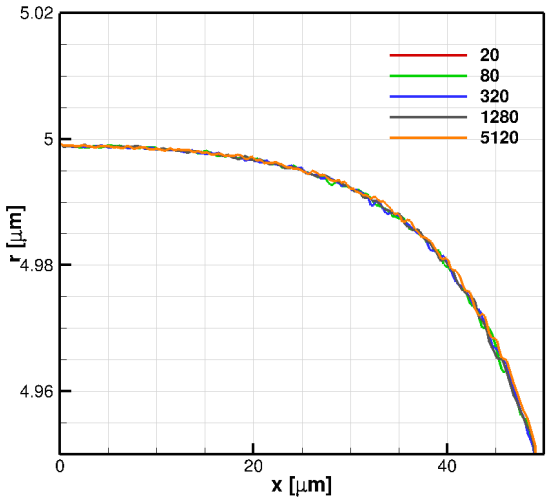

Figure 4.8: Effect of coupling frequency on the predicted shape of the fiber. The different lines are for different choice of coupling interval.

Based on this analysis it can be surmised that the surface reconstruction and coupling algorithm are very efficient, and that in general both the results of the simulation as well as the overall cost are insensitive to this choice. A "conservative" choice of coupling interval of 200 is used going forward.

Effect of reaction mechanism

Now the effect of the oxidation mechanism is examined. Figure 4.9 shows the evolution of the fiber radius for the $O_2 + C(s) \rightarrow CO_2$ reaction mechanism for wall temperatures of 800K (*left*) and 1300K (*right*). The dominant feature of these simulations is that the fiber radius remains relatively uniform over time. Uniform "thinning" is typical when the reaction rate is small compared to the fluidic time scales (in this case diffusion). The fiber essentially "sees" a uniform flux of reactant for the duration of the simulation and there is little to no feedback to the fluid from the change in shape of the fiber. This is the so-called *reaction limited* regime.

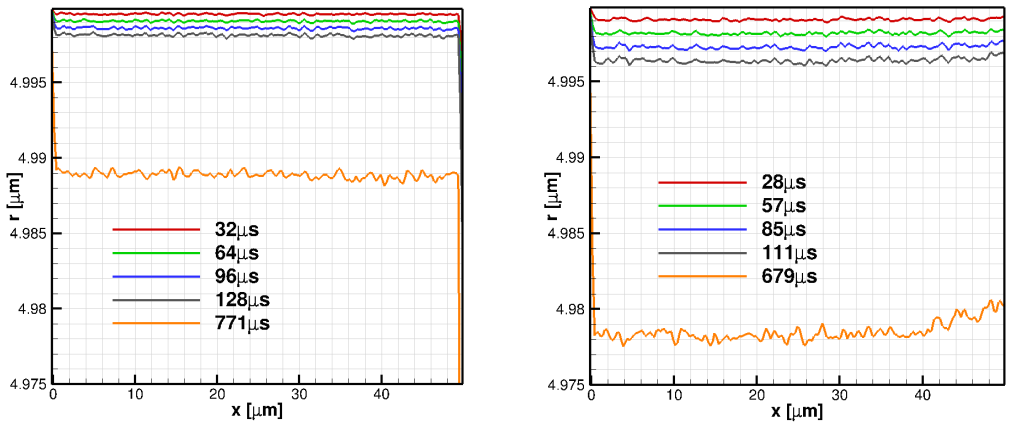

Figure 4.9: Predicted fiber profiles at various times for test case 1 (*left*) and 3 (*right*) from table 4.1.

In contrast, Fig. 4.9 shows the evolution of the fiber radius for the $O + C(s) \rightarrow CO$ reaction mechanism for wall temperatures of 800K (*left*) and 1300K (*right*). In this case, the thinning is more pronounced near the top of the fiber resulting in the onset of the "needled" morphology. This is typical of the *diffusion limited* oxidation regime. In this case the time scales of surface reaction are of the order, or greater than the time scale of the diffusion of reactants through the gas. Therefore reactions near the top of the fiber consume the majority of available reactants and choke off the supply of reactants to the lower portion of the fiber.

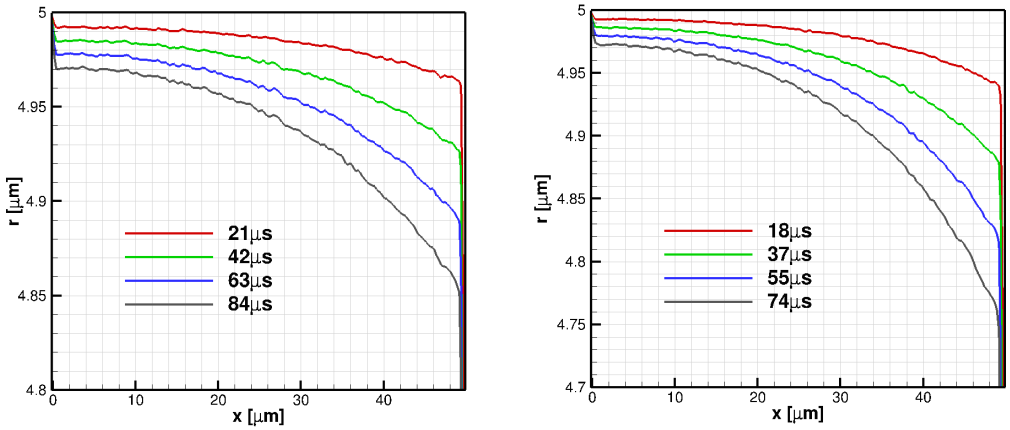

Figure 4.10: Predicted fiber profiles at various times for test case 2 (*left*) and 4 (*right*) from table 4.1.

It is important to note that there is another factor which regulates the reaction in these cases and that is the rate of diffusion of reactant through the reactant-product gas mixture. Because in this case the disparity in reaction rates is so great, it can be assumed to be the dominant factor in the differences observed in the fiber evolution. In a subsequent section, the effect of differential diffusion will be isolated by setting the reaction probabilities to be equal.

We can begin to assess the comparative efficiency of of each system in removing carbon by looking at the rate of ablation. Figure 4.11 shows the mass loss rates for each system at each temperature as a function of time.

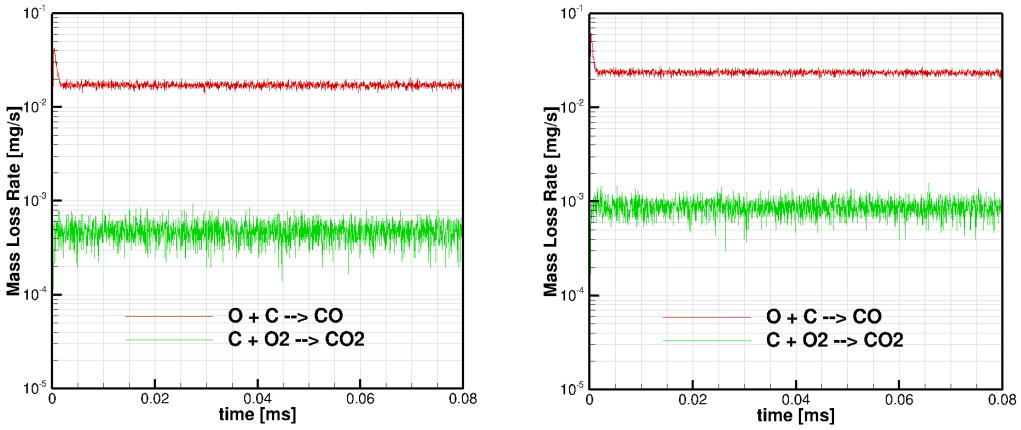

Figure 4.11: Mass loss rates of solid carbon as a function of time for test cases 1 and 2 (*left*), and cases 3 and 4 (*right*)

Based on the mass loss rates from these simulations, a preliminary estimate of the cost of performing coupled ablating simulations of real microstructures at *relevant* scales can be derived. For the type of analysis we would wish to do using the methodology proposed in this work it will be important to be able to simulate a representative volume element (RVE). What constitutes a valid RVE will vary based on the material, however for the purposes of this discussion let us suppose that a 1mm $\times$ 1mm $\times$ 1mm cube is representative. The FiberForm material that has been investigated previously has a density of . Based on the calculations preformed in this section, the computational cost per mass of ablating the microstructure is . Therefore, the estimated cost for fully ablating 1mm^3 of a FiberForm-like microstructure would be . Or, put another way, it would require approximately days on 1000 CPU's.

4.2 Simulations of Ablating Microstructures

We would now like to apply this coupled methodology to more complicated microstructures composed of many fibers to better understand the interaction of the ablation

process with the porous medium, as well as investigate the effect of various modeling parameters.

4.2.1 Test Case Set-up

For these purposes, another test case is proposed. An illustration of the simulation domain and microstructure is seen in Fig. 4.12. Reactant species (either O or O_2) diffuse in from the left side of the domain. At the right side of the domain is a non-reacting non-thermal wall. On all other boundaries a symmetry boundary condition it applied. The microstructure, which fills the right half of the domain has a nominal porosity of 0.9 in all cases. Though the fiber generation code developed in Chapter 2 can create fibers with a distribution of diameters, here the fiber diameter is prescribed as a constant 10μm.

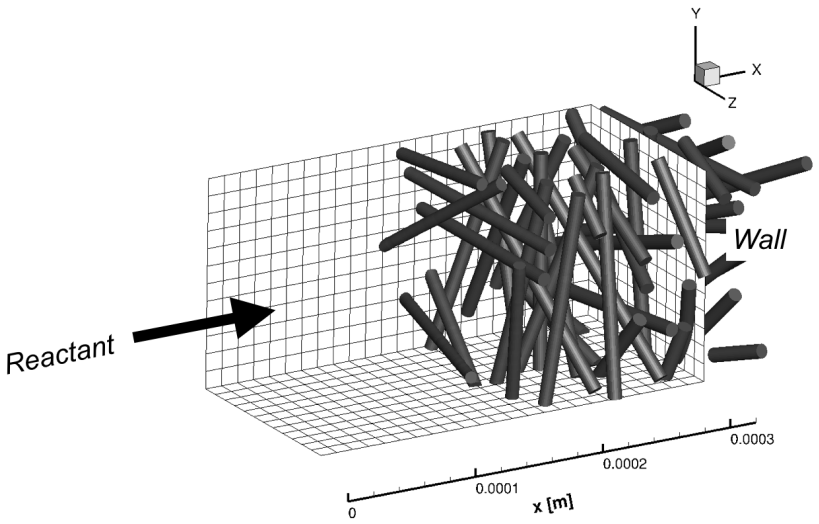

Figure 4.12: Illustration of the simulation setup for the microstructure simulations.

With this test case we would like to investigate the effect of various aspects of this problem in isolation. Therefore the reaction probability, α, is prescribed to arbitrary values, in these cases 1.0 and 0.1. The matrix of test conditions used in this part of the

study is shown in Table 4.2. Here, the Knudsen number, Kn_D, is defined as the ratio of the mean free path of the gas to fiber diameter ($Kn_D = \lambda/D$).

Case	Microstructure	Reactant	Product	α	Kn_D
1	1	O	CO	0.1	1.90
2	1	O	CO	1.0	1.90
3	1	O_2	CO_2	0.1	1.90
4	1	O_2	CO_2	1.0	1.90
5	2	O_2	CO_2	0.1	1.90
6	2	O_2	CO_2	1.0	1.90
7	1	O	CO	1.0	0.80

Table 4.2: Test matrix for the coupled microstructure simulations presented in this section.

In the subsequent sections in this chapter the results from these simulations will be used to investigate the influence of various physical properties, including the gas-surface reaction rate, the chemical species, the mean free path of the gas, and the microstucture.

4.2.2 Simulation Results

Figures 4.13 – 4.16 show results from simulations of cases 1 – 4 from Table 4.2. In all figures, the image on the left shows contours of mole fraction of reactant, as well as a visualization of the ablated microstructures. The image on the right plots the individual element radii normalized by the nominal initial radius as a function of depth. The dashed line in this figure shows the location of the back wall in the simulation. For these four cases the results are plotted after 4.53μs (*top*), 45.29μs (*middle*), and 90.58μs (*bottom*).

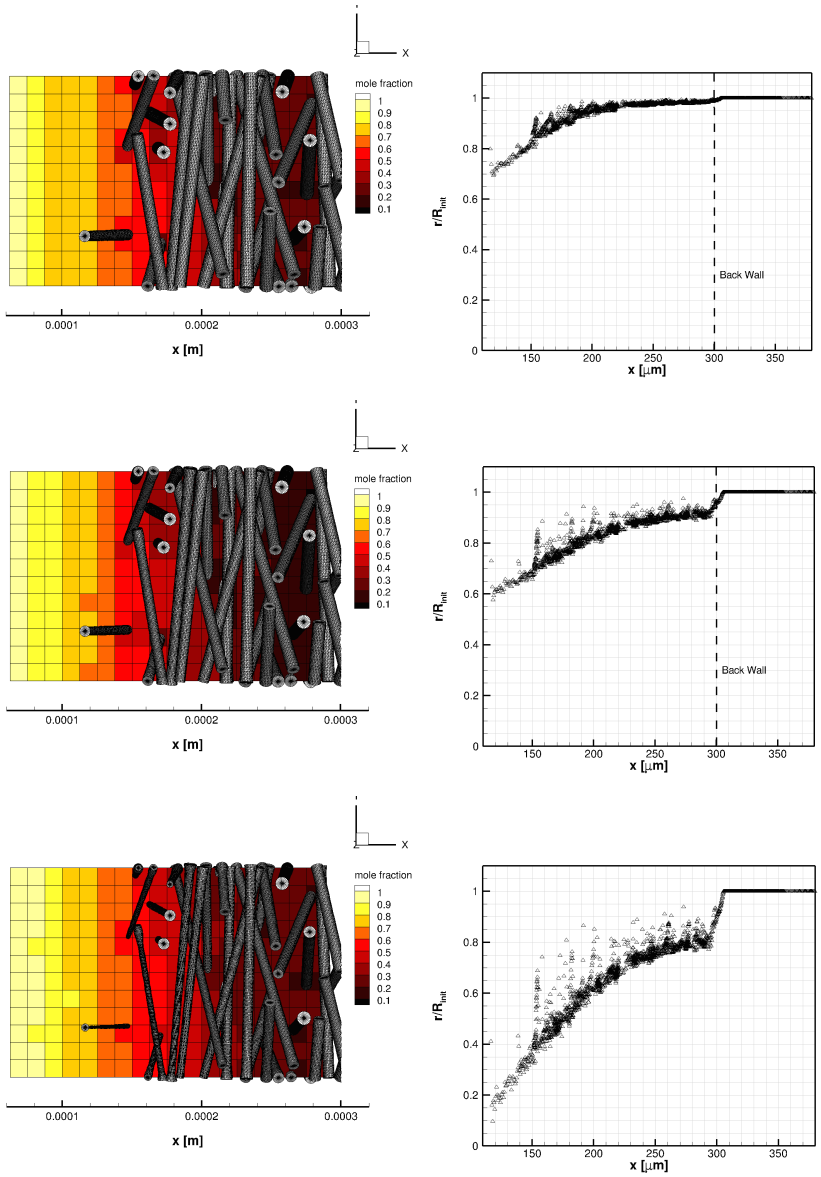

Figure 4.13: Visualization (*left*) and element radii as a function of depth (*right*) for test case 1 after $4.53\mu s$ (*top*), $45.29\mu s$ (*middle*), and $90.58\mu s$ (*bottom*).

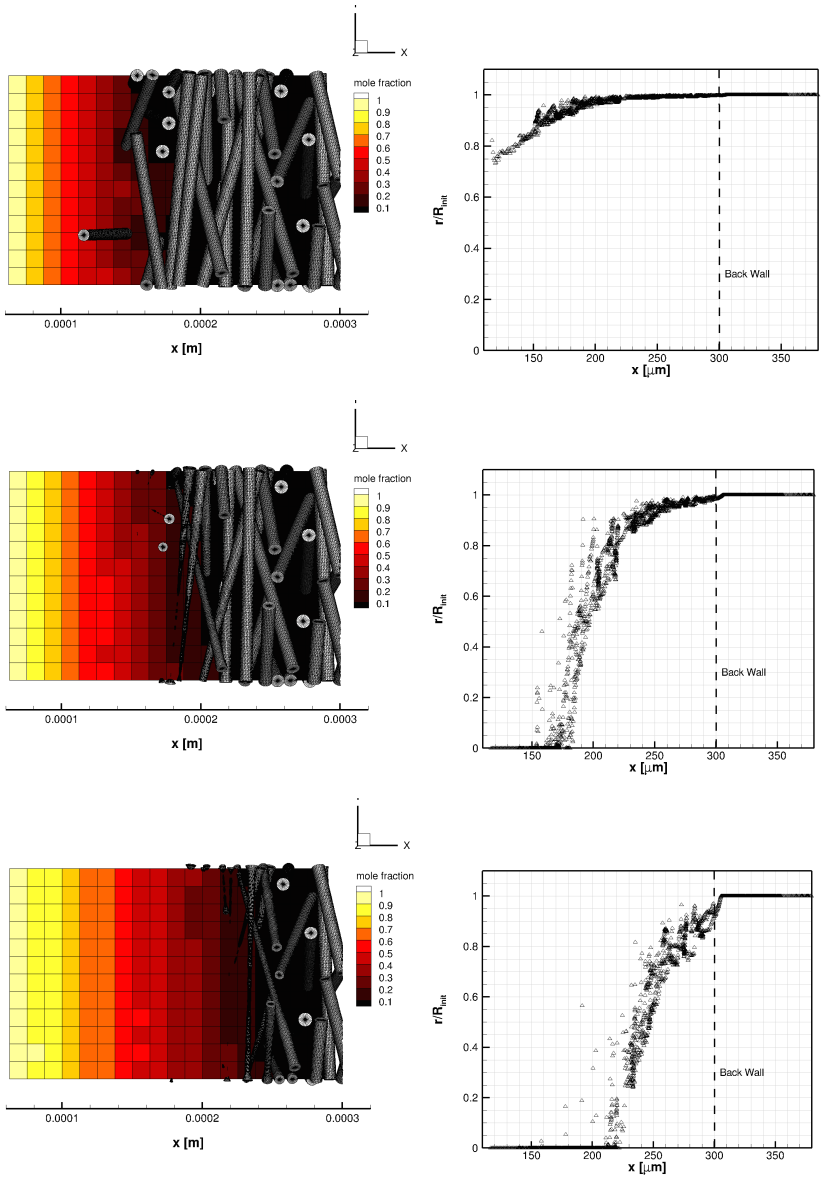

Figure 4.14: Visualization (*left*) and element radii as a function of depth (*right*) for test case 2 after $4.53\mu s$ (*top*), $45.29\mu s$ (*middle*), and $90.58\mu s$ (*bottom*).

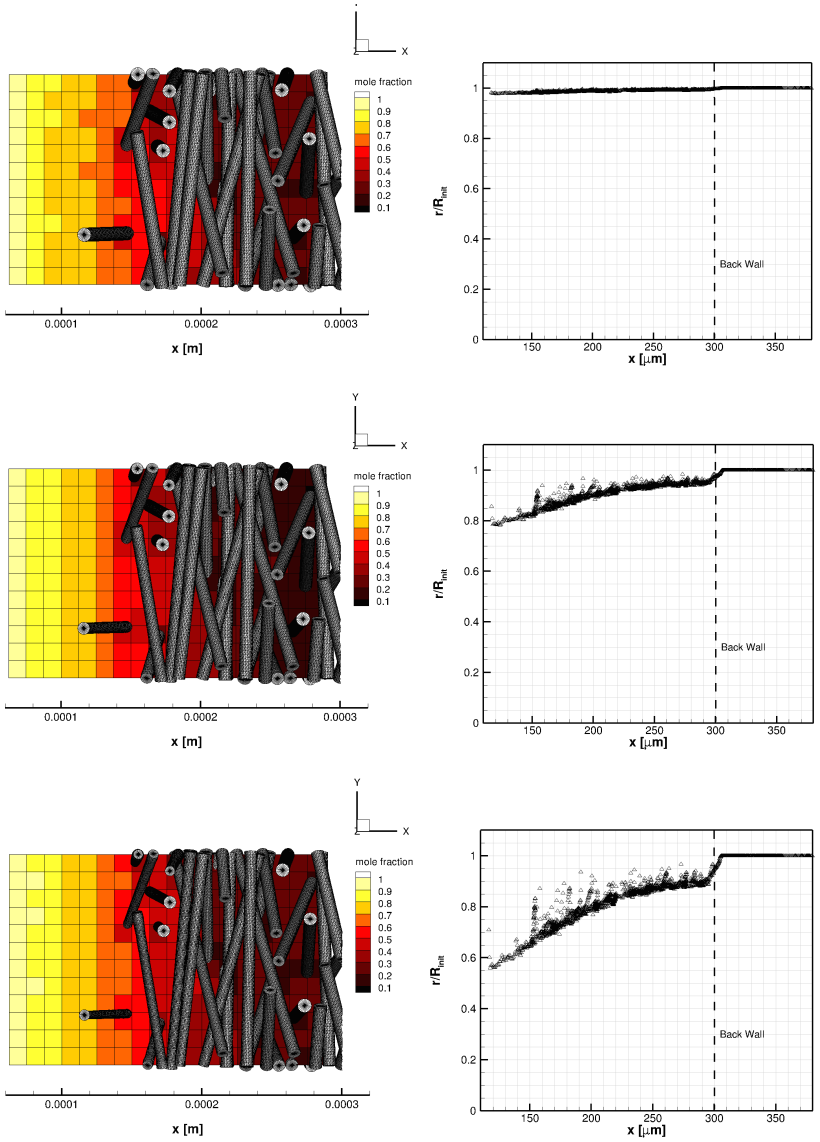

Figure 4.15: Visualization (*left*) and element radii as a function of depth (*right*) for test case 3 after $4.53\mu s$ (*top*), $45.29\mu s$ (*middle*), and $90.58\mu s$ (*bottom*).

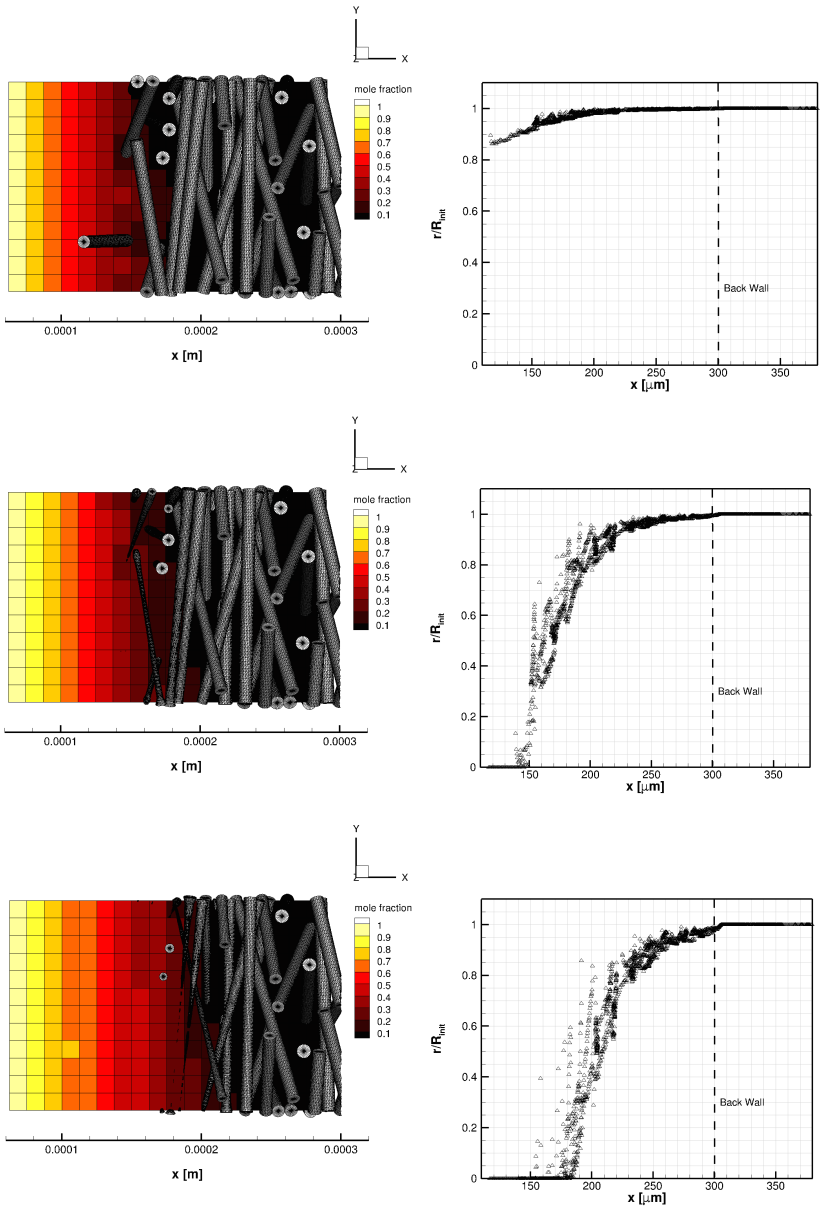

Figure 4.16: Visualization (*left*) and element radii as a function of depth (*right*) for test case 4 after $4.53\mu s$ (*top*), $45.29\mu s$ (*middle*), and $90.58\mu s$ (*bottom*).

Effect of reaction rate

The first modeling parameter that will be investigated in this section is the reaction probability α. Figure 4.17 shows plots of normalized element radii as function of depth, where in each case the microstructure and reaction mechanism has been held constant, but the reaction probability has been varied. In these cases, the "fast" probability corresponds to $\alpha = 1.0$ and the "slow" probability corresponds to value of $\alpha = 0.1$.

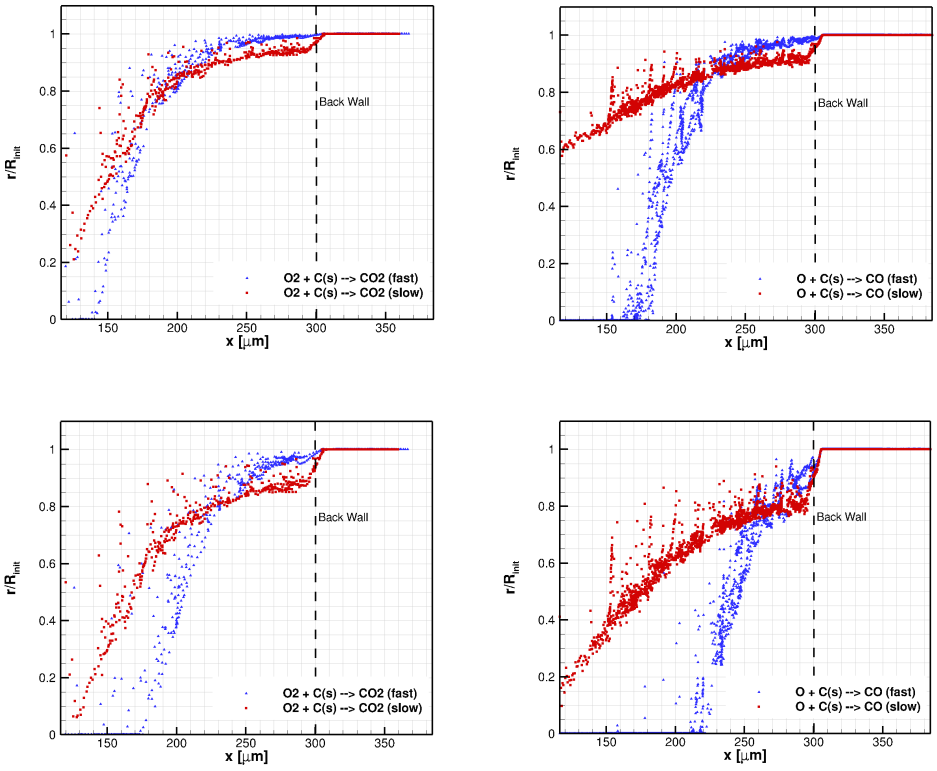

Figure 4.17: Effect of reaction probability on element radius in-depth. The left figures are for the molecular oxygen setup, and the right figures are for the atomic oxygen setup. The top figures are after 45.29μs, and the bottom figures are after 90.58μs.

For both the O and O_2 pathways, a fundamentally different evolution of the microstructure in-depth emerges. Focusing on the plots for the O pathway (case 1 and 2), a distinctly different fiber radius distribution is observed. For the "fast" reaction probability there is a more precipitous drop-off in radius near the left side of the microstructure. In cases with a "slow" reaction probability there is a more flat distribution of radii. It is also interesting to note that there is in fact greater thinning of the fibers in-depth with the slower reaction probability. The reason for this is the same as for the single fiber cases presented in the previous section. That is, the fast reaction probability is simultaneously consuming reactant before it can penetrate deeper in the microstructure, as well as producing more product which inhibits the diffusion of reactant into the microstructure.

Effect of Chemical Species

In Fig. 4.17 there is also an observed difference when the plots for the two different reaction pathways are compared. The difference between the fiber radii for the O and O_2 pathways are compared directly in Fig. 4.18. In this figure, the plots on the left are for the slow reaction probability at two different simulation times, and the right plots show the fast reaction probabilities at two different times.

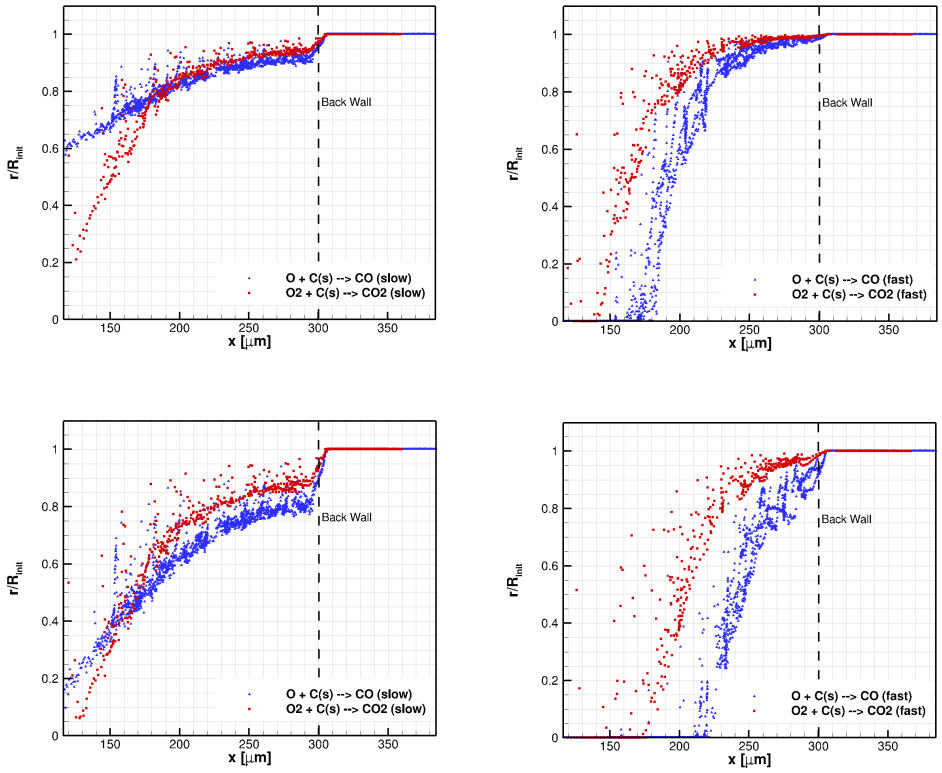

Figure 4.18: Effect of chemical species on element radius in-depth. The left figures are for the molecular oxygen setup, and the right figures are for the atomic oxygen setup. The top figures are after 45.29μs, and the bottom figures are after 90.58μs.

In all cases – as well as in the previous figure – a more diffusion limited character in the microstructure morphology is observed for the O_2 reaction pathway, meaning that more pronounced ablation is observed near the exposed "surface" (*left side*) of the microstructure than in-depth. This is explained by the differences in effective diffusion rates for the two different pairs of species. In the case of the O_2 reaction pathway, both the reactant as well as the medium through which it diffuses contain heavier molecules which attenuates the rate of diffusion. Thus the characteristic time scale of diffusion is reduced in comparison with that of reaction, which for this examination is held constant.

Effect of Mean Free Path

The effect of the mean free path of the gas on the ablation characteristics of the microstructure has also been investigated. As the mean free path – and therefore the Knudsen number – is decreased, collisions between gas particles (in this case O atoms) have a greater effect on the diffusion. In contrast, when the Knudsen number is increased, we would expect the interactions of the gas particles with the surfaces of the microstructure to become more important.

Figure 4.19 shows a comparison of in-depth element radii between case 2 and case 7 from table 4.2. For these two test cases, the gas pressure was held constant at 0.04 atm, however, the mean free path was decreased for case 7 by decreasing the temperature of the gas. In this plot, we can see the expected behavior that with an increase in Knudsen number, there is enhanced diffusion and therefore slightly greater penetration of reactant gas into the microstructure.

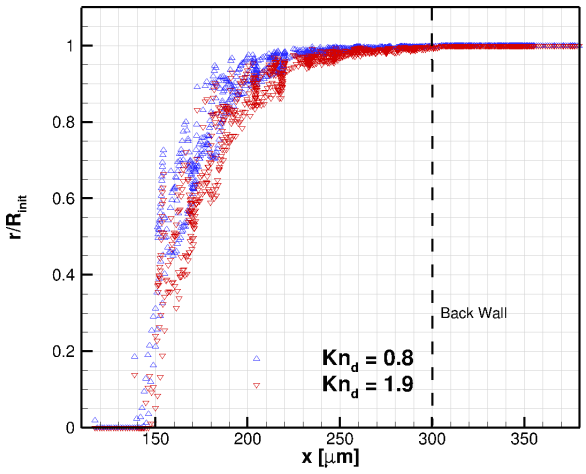

Figure 4.19: Effect of mean free path on in-depth element radii.

Effect of Microstructure

Finally, because the random microstructure used in the previous studies is unique, the effect of using a *different* random microstructure is also investigated. Figure 4.20 shows visualizations of the two random microstructures used in this investigation.

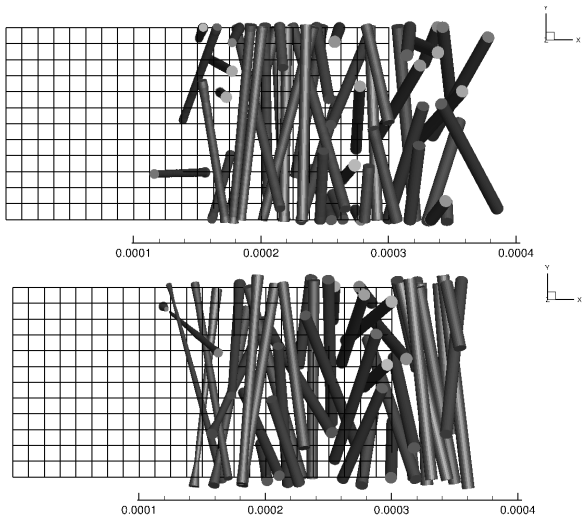

Figure 4.20: Two different random microstructures used for comparison. The top is referred to in table 4.2 as Microstructure 1, and the bottom is Microstructure 2. The both have a nominal porosity of 0.90.

In Fig. 4.21 the element radii as a function of depth is presented for the two microstructures for both the slow reaction probability (*left*), and the fast reaction probability (*right*). In these figures it is observed that for the slow reaction probability, there is a difference in in-depth fiber radii, whereas for the fast reaction probability case, there is little observable difference. From this it is concluded that, in the reaction limited regime, *actual* micro-structural geometry has more of an effect, than in the diffusion limited regime where the ablation is largely confined to the surface. For these cases, it is only the bulk porosity which has been held constant, but the actual pore sizes and distribution may vary. This apparently will have an effect on the rate of diffusion of

reactant into the microstructure.

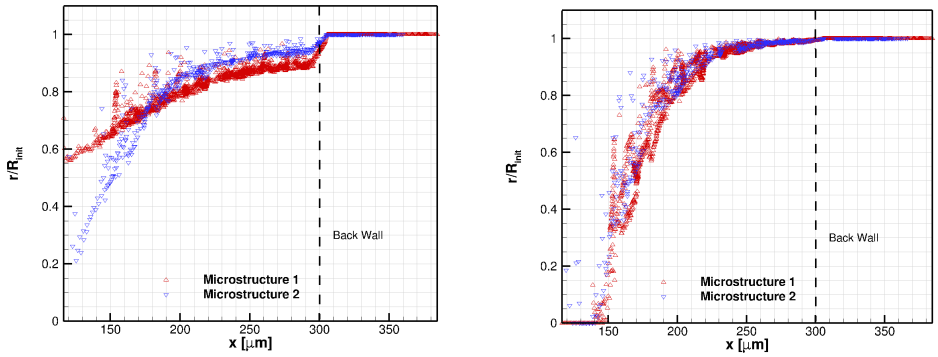

Figure 4.21: Comparison of element radii for the two different microstructures seen in fig. 4.20. The figure on the left is for $\alpha = 0.1$ and the figure on the right is for $\alpha = 1.0$.

Concluding remarks

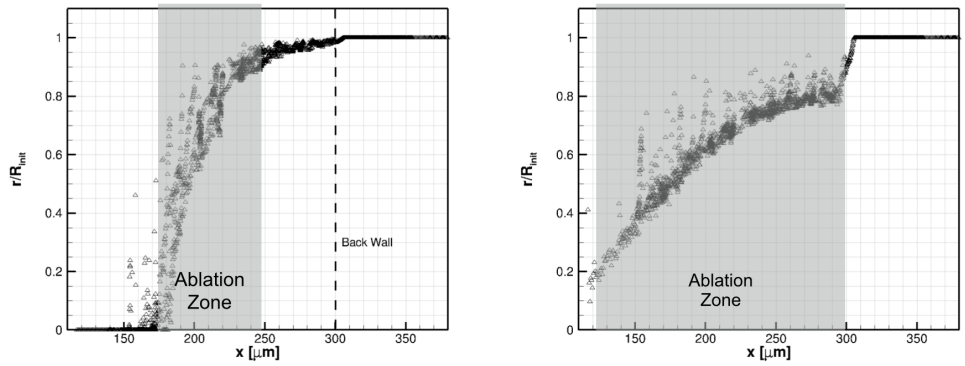

Figure 4.22: Illustration of the volumetric ablation phenomenon for a diffusion limited regime (*left*) and reaction limited regime (*right*).

From these analyses, it is concluded that various physical modeling parameters will have an impact on the ablative behavior of a porous microstructure. Depending on the gas-surface interaction mechanism, the molecular properties of the gas, the microstructure,

or the mean free path, the ablation process may be largely considered to be a surface phenomenon, *or* it may occur in-depth. As stated in chapter 1, engineering models for ablative TPS materials that are in use today typical confine the ablation process to the surface. Based on the analysis such as that presented in this chapter, one could in principal conceive of new macroscopic models which take into account the ablation of the the microstructure in-depth and perhaps improve the fidelity of the prediction.

Chapter 5

Conclusions and Future Work

5.1 Conclusions

A new approach for modeling the flow through porous spacecraft TPS materials has been presented. This approach uses the DSMC method to account for all of the relevant flow physics at the microscale. To the author's knowledge, at the time of this writing, this is the first time the DSMC method has been applied to microscale ablation modeling. Additionally, a method for producing simulated fibrous microstructures has also been presented. Finally a new method for moving the surface of the simulant microstructures has been developed. This method is shown to be robust and efficient for simulating the in-depth ablation of thermal protection system materials.

This new approach was first applied to simulating non-reacting flow through porous media, such as those found in spacecraft TPS. Validation cases for idealized geometries have shown good agreement with an empirical relationship from the literature, as well as CFD predictions. Predicting permeability for more realistic materials using this method shows promise, however, dispersion in the experimental data we have compared to make definite conclusions about the method's efficacy difficult. This highlights the need for new permeability measurements of modern FiberForm®.

Simulations of the in-depth ablation due to oxidation of simulant porous microstructures illuminate how differences in physical modeling parameters can produce fundamentally different morphologies after ablation. For example, when the reaction rate for the heterogeneous reaction is low compared to the rate of diffusion of reactant, the reactants will penetrate deeper into the microstructure and the ablation of the bulk is volumetric. In contrast, if the reaction rate is high, the rate of ablation of the bulk is limited by the diffusion of reactants to the surface of the microstructure. In these cases the ablation of the bulk is more or less confined to the surface of the geometry. Similar qualitative conclusions have been drawn for the effect of the Knudsen number, as well as chemical composition.

5.2 Future Work

As mentioned previously, the work presented here represents a first step in applying this method to the modeling of spacecraft TPS. As such, there remains a great deal of work to be done before this approach can yield substantive improvement advancement in the predictive capability of ablator response models. In the following two sections, two areas of future work will be highlighted.

5.2.1 Modeling

The current work, in the interest of validating an approach which has largely not been applied to this problem, simple physical systems were used (i.e Carbon-Oxygen). In the case of a realistic ablative TPS material, the physical system is in general very complex. Perhaps the most notable difference between the systems examined in the current work, and those found in a typical ablative TPS material, is the absence of the organic resin. Lightweight pyrolyzing ablators, as discussed in Ch.1, typically are impregnated with an organic resin; phenolic in the case of the material PICA. The decomposition of the resin provides a great deal of the h energy dissipation effect which makes ablative TPS

attractive. The current work has not included these materials, however for this approach to be useful in the general case, the presence of the resin should be accounted for.

Since the resin in the real material occupies the voids between the fibers, the methodology for building the microstructure and moving the surface would not be applicable in the same way to the decomposition of the resin. An approach for tracking of a general interface, such as a marching cubes[34] coupled to a volume of fluid (VOF) approach [54], would likely be more desirable in this case. Further difficulty will arise from the large increase in the number of chemical species that must be accounted for when there is decomposition of a complex organic polymer. Several studies[55],[56] have been performed on developing a reduces in chemistry model for the carbon-phenolic-air system, and their reduced models typically include $\approx$ 20 species. This will result in a large increase in the cost and complexity of the DSMC simulation. It is the opinion of this author that a significant investment in research effort must be made in order to address this issue and enable application of this method to more realistic problems.

5.2.2 Microtomography

Finally, one of the attractive features of DSMC, and the *MGDS* implementation in particular, is that it can accommodate geometry of any complexity. This enables a compelling application for this methodology: simulating *real* microstructures obtained from doing X-ray computed micro-tomography scans of the materials. Micro-tomography has previously been applied to spacecraft heatshield analysis by Mansour et al.[57]. Using high-resolution scans of FiberForm, Mansour et al. characterized some of the parameters of the microstructure. Additionally, they used the random walk approach of Lachaud et al.[3] to simulate the ablation of the microstructure under certain conditions. Taking a similar approach, but using DSMC, allows for more of the relevant physics to be simulated.

As a demonstration for this work, we have scanned a small sample of FiberForm using the X5000 high resolution microCT system at the X-ray computed tomography lab at

the University of Minnesota. This system has a maximum resolution of approximately 2μm The output from a tomography scan is typically a stack of grayscale images, each corresponding to a slice of the material. A visualization of this can be seen in the left half of Fig. 5.1. These images are then filtered. Finally a threshold grayscale value is identified that corresponds to the surface, and images are converted to binary (black and white). From here we can construct a triangulated surface corresponding to the threshold value. For this demonstration the triangulation was performed using the Avizo software package. A rendering for a 1mm by 1mm volume of the material is shown on the right half of Fig. 5.1.

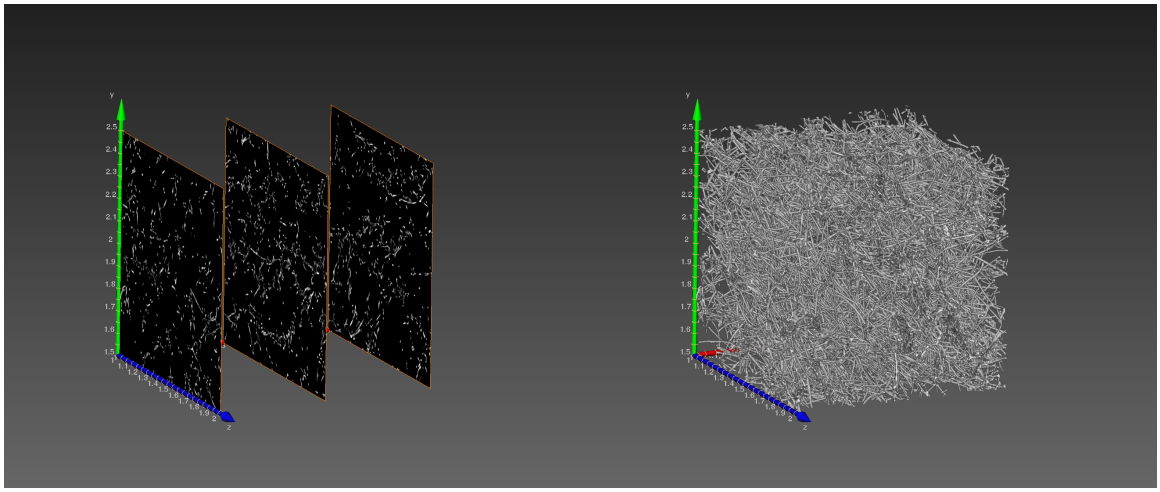

Figure 5.1: Example outputs from the tomographic scan. The left image shows three gray scale TIFF images and the right is a rendering of the isosurface corresponding to a grayscale value of 62.

Using the triangulated surface obtained from the tomographic scan, we can now simulate the flow through material using the method described in this and the previous work[58]. Figure 5.2 show some slices from a simulation through a tomographic surface. In these simulations, Dirichlet boundary conditions have been imposed at the inflow and the outflow, with a constant velocity of 1 m/s. This is not properly physical

for the realistic situation, however our purpose here to demonstrate the viability of the approach. In the results from the simulation we can see that the flow accelerates through the consolidated pores in the microstructure and stagnates where there is a blockage.

An important feature of the *MGDS* code that enables these simulations is that the surface is partitioned across multiple processors just as is the flow mesh. This is necessary due to the extremely large amount of triangles required to define these surfaces. Figure 5.3 shows a simulation with the same conditions as above, but for a larger volume element. The surface shown in this image contains over 24 million triangles.

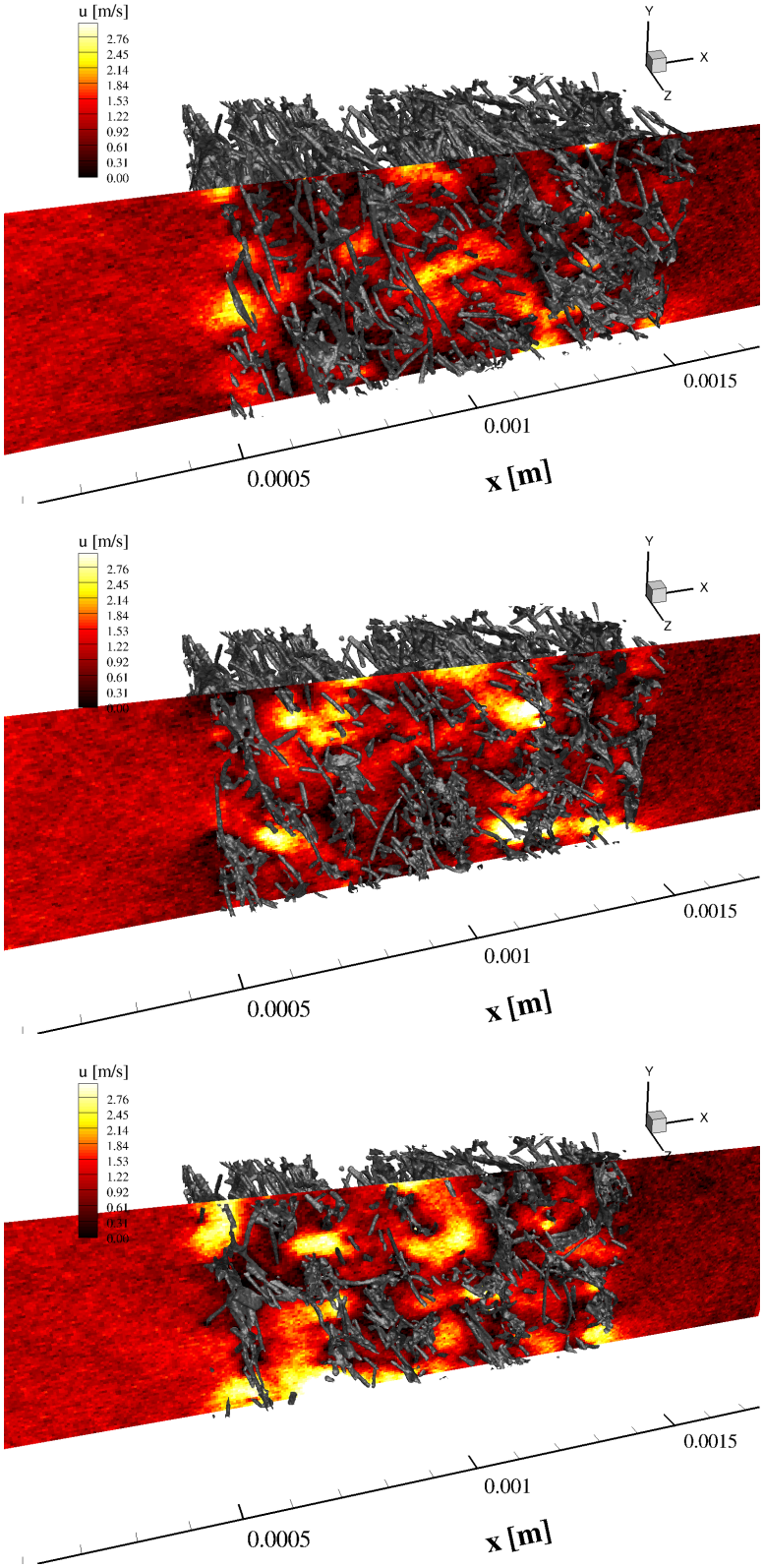

Figure 5.2: Slices for the flow of N_2 through FiberForm. The microstructure used in these simulations was obtained using micro-tomography.

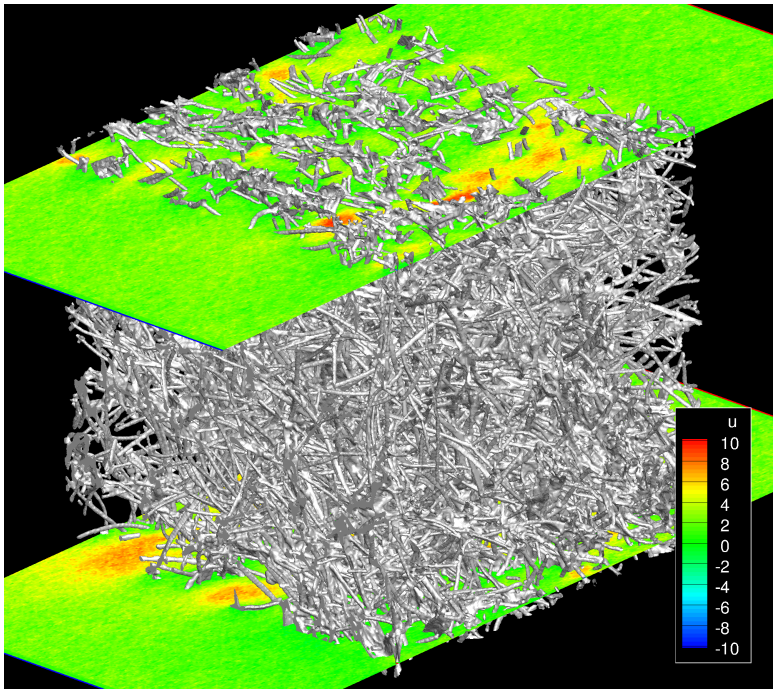

Figure 5.3: Simulation results of the full 1mm^3 volume. The surface in this simulation is composed of ≈ 24 million triangles.

These simulations demonstrate the important conclusion that the approach developed in the current work, when applied with a state-of-the-art DSMC implementation such as MGDS, can simulate a real spacecraft TPS microstructure at a relevant scale and relevant conditions. Future work will be performed to validate these microstructures for porous media flow using the same procedure as was used for the simulant microstructures in Ch. 3. The cost of scanning one of these materials is comparatively inexpensive, so the prospect of being able to simply scan the material and then immediately perform physics-based simulations on the microstructure would have significant impact on the TPS modeling community.

References

[1] Y. K. Chen and Frank S. Milos. Ablation and Thermal Response Program for Spacecraft Heatshield Analysis. *Journal of Spacecraft and Rockets*, 36(3):1–9, May 1999.

[2] Adam J. Amar, Bennie F Blackwell, and J R Edwards. Development and Verification of a One-Dimensional Ablation Code Including Pyrolysis Gas Flow. *Journal of Thermophysics and Heat Transfer*, 23(1):59–71, January 2009.

[3] Jean Lachaud, Ioana Cozmuta, and Nagi N. Mansour. Multiscale Approach to Ablation Modeling of Phenolic Impregnated Carbon Ablators. *Journal of Spacecraft and Rockets*, 47(6):910–921, November 2010.

[4] Mairead Stackpoole, Steve Sepka, Ioana Cozmuta, and Dean A. Kontinos. Post-Flight Evaluation of Stardust Sample Return Capsule Forebody Heatshield Material. In *46th AIAA Aerospace Sciences Meeting*, pages 1–7, Reno, January 2008.

[5] J Lachaud and G L Vignoles. A Brownian motion technique to simulate gasification and its application to C/C composite ablation. *Computational Materials Science*, 44(4):1034–1041, February 2009.

[6] Jean Lachaud and Nagi N. Mansour. Microscopic scale simulation of the ablation of fibrous materials. In *49th AIAA Aerospace Sciences Meeting*, pages 1–35, Orlando, January 2010.

[7] Chonglin Zhang and Thomas E Schwartzentruber. Robust cut-cell algorithms for DSMC implementations employing multi-level Cartesian grids. *Computers and Fluids*, 69(C):122–135, October 2012.

[8] Chunpei Cai, Iain D Boyd, Jing Fan, and Graham V Candler. Direct Simulation Methods for Low-Speed Microchannel Flows. *Journal of Thermophysics and Heat Transfer*, 14(3):368–378, July 2000.

[9] S L Lee and J H Yang. Modeling of Darcy-Forchheimer drag for fluid flow across a bank of circular cylinders. *International Journal of Heat and Mass Transfer*, 40(13):3149–3155, 1997.

[10] Francesco Panerai, Alexandre Martin, Nagi N. Mansour, Steven A Sepka, and Jean Lachaud. Flow-Tube Oxidation Experiments on the Carbon Preform of a Phenolic-Impregnated Carbon Ablator. *Journal of Thermophysics and Heat Transfer*, 28(2):181–190, April 2014.

[11] Jochen Marschall and Frank S. Milos. Gas Permeability of Rigid Fibrous Refractory Insulations. *Journal of Thermophysics and Heat Transfer*, 12(4):528–535, October 1998.

[12] Chul Park. Effects of atomic oxygen on graphite ablation. *AIAA Journal*, 14(11):1640–1642, 1976.

[13] Chul Park. *Nonequilibrium Hypersonic Aerothermodynamics*. 1990.

[14] Kenneth L. Atkins, Donald E. Brownlee, Tom Duxbury, Chen-wan Yen, Peter Tsou, and Joseph M. Velliaga. STARDUST: Discovery's Interstellar Dust Cometary Sample Return Mission. pages 1–17, February 2004.

[15] Dean A. Kontinos and Mairead Stackpoole. Post-Flight Analysis of the Stardust Sample Return Capsule Earth Entry. In *46th AIAA Aerospace Sciences Meeting*, pages 1–14, Reno, January 2008.

[16] Huy Tran, Christine Johnson, Daniel Rasky, Frank Hui, Ming-Ta Hsu, and Y Chen. Phenolic Impregnated Carbon Ablators (PICA) for Discovery class missions. In *31st Thermophysics Conference*, pages 1–15, New Orleans, June 1996.

[17] R. J. Schoner. CMA Manual. Technical Report UM-70-14, April 1970.

[18] Carl B Moyer and Roald A Rindall. An Analysis of the Coupled Chemically Reacting Boundary Layer and Charring Ablator, Part II: Finite Difference Solution for the In-Depth Response of Charring Materials Considering Surface Chemical and Energy Balances, 1968.

[19] Frank S. Milos and Y. K. Chen. Two-Dimensional Ablation, Thermal Response, and Sizing Program for Pyrolyzing Ablators. *Journal of Spacecraft and Rockets*, 46(6):1089–1099, November 2009.

[20] Yih-Kanq Chen and Frank Milos. Three-Dimensional Ablation and Thermal Response Simulation System. In *38th AIAA Thermophysics Conference*, pages 1–16, Toronto, June 2005.

[21] Y. K. Chen, Frank S. Milos, and Tahir Gökçen. Validation of a Three-Dimensional Ablation and Thermal Response Simulation Code. In *10th AIAA/ASME Joint Thermophysics and Heat Transfer Conference*, pages 1–14, Chicago, July 2010.

[22] Adam J. Amar, Bennie F Blackwell, and Jack R Edwards. One-Dimensional Ablation Using a Full Newton's Method and Finite Control Volume Procedure. *Journal of Thermophysics and Heat Transfer*, 22(1):71–82, January 2008.

[23] Alexandre Martin and Iain D Boyd. Strongly coupled computation of material and nonequilibrium flow for hypersonic ablation. In *41st AIAA Thermophysics Conference*, pages 1–15, San Antonio, June 2009.

[24] Alexandre Martin and Iain D Boyd. Mesh tailoring for strongly coupled computation of ablative material in nonequilibrium hypersonic flow. In *10th AIAA/ASME*

Joint Thermophysics and Heat Transfer Conference, pages 1–16, Chicago, June 2010.

[25] Stephen Whitaker. Flow in porous media I: A theoretical derivation of Darcy's law. *Transport in porous media*, 1(1):3–25, 1986.

[26] Alexandre Martin and Iain D Boyd. Non-Darcian Behavior of Pyrolysis Gas in a Thermal Protection System. *Journal of Thermophysics and Heat Transfer*, 24(1):60–68, January 2010.

[27] Hyo-Keun Ahn, Chul Park, and Keisuke Sawada. Response of Heatshield Material at Stagnation Point of Pioneer-Venus Probes. *Journal of Thermophysics and Heat Transfer*, 16(3):1–8, July 2002.

[28] Haoyue Weng and Alexandre Martin. Multidimensional Modeling of Pyrolysis Gas Transport Inside Charring Ablative Materials. *Journal of Thermophysics and Heat Transfer*, pages 1–15, August 2014.

[29] Yih-Kanq Chen and Frank S. Milos. Effects of Nonequilibrium Chemistry and Darcy—Forchheimer Pyrolysis Flow for Charring Ablator. *Journal of Spacecraft and Rockets*, 50(2):256–269, March 2013.

[30] Georges Duffa, Gerard L Vignoles, Jean-Marc Goyhénèche, and Yvan Aspa. Ablation of carbon-based materials: Investigation of roughness set-up from heterogeneous reactions. *International Journal of Heat and Mass Transfer*, 48(16):3387–3401, July 2005.

[31] Gerard L Vignoles, Jean Lachaud, Yvan Aspa, and Jean-Marc Goyhénèche. Ablation of carbon-based materials: Multiscale roughness modelling. *Composites Science and Technology*, 69(9):1470–1477, July 2009.

[32] G L Vignoles, Y Aspa, and M Quintard. Modelling of carbon–carbon composite ablation in rocket nozzles. *Composites Science and Technology*, 70(9):1303–1311, September 2010.

[33] G L Vignoles. Modelling Binary, Knudsen and Transition Regime Diffusion Inside Complex Porous Media. *Le Journal de Physique IV*, 05(C5):C5–159–C5–166, June 1995.

[34] Gerard L Vignoles, Marc Donias, Christianne Mulat, Christian Germain, and Jean-François Delesse. Simplified marching cubes: An efficient discretization scheme for simulations of deposition/ablation in complex media. *Computational Materials Science*, 50(3):893–902, January 2011.

[35] Albert Einstein. *Investigations on the Theory of the Brownian Movement*. Courier Corporation, 1956.

[36] Alexandre Martin. Volume averaged modeling of the oxidation of porous carbon fiber material. In *44th AIAA Thermophysics Conference*, San Diego, California, June 2013.

[37] G A Bird. *Molecular Gas Dynamics and the Direct Simulation of Gas Flows*. Oxford University Press, 1994.

[38] Wolfgang Wagner. A convergence proof for Bird's direct simulation Monte Carlo method for the Boltzmann equation. *Journal of Statistical Physics*, 66(3-4):1011–1044, 1992.

[39] Walter G. Vincenti and Charles H Kruger. *Introduction to Physical Gas Dynamics*. 1965.

[40] G J LeBeau. A parallel implementation of the direct simulation Monte Carlo method. *Computer Methods in Applied Mechanics and Engineering*, 174(3):319–337, 1999.

[41] Stefan Dietrich and Iain D Boyd. Scalar and parallel optimized implementation of the direct simulation Monte Carlo method. *Journal of Computational Physics*, 126(2):328–342, 1996.

[42] Da Gao, Chonglin Zhang, and Thomas E Schwartzentruber. Particle Simulations of Planetary Probe Flows Employing Automated Mesh Refinement. *Journal of Spacecraft and Rockets*, 48(3):397–405, May 2011.

[43] Ioannis Nompelis and Thomas Schwartzentruber. A Parallel Implementation Strategy for Multi-Level Cartesian Grid Based DSMC Codes. In *51st AIAA Aerospace Sciences Meeting including the New Horizons Forum and Aerospace Exposition*, Grapvine, TX, January 2013.

[44] Moran Wang and Zhixin Li. Simulations for gas flows in microgeometries using the direct simulation Monte Carlo method. *International Journal of Heat and Fluid Flow*, 25(6):975–985, December 2004.

[45] Quanhua Sun and Iain D Boyd. Evaluation of Macroscopic Properties in the Direct Simulation Monte Carlo Method. *Journal of Thermophysics and Heat Transfer*, 19(3):329–335, July 2005.

[46] Robert P Nance, David B Hash, and H A Hassan. Role of Boundary Conditions in Monte Carlo Simulation of Microelectromechanical Systems. *Journal of Thermophysics and Heat Transfer*, 12(3):447–449, July 1998.

[47] K Yazdchi, S Srivastava, and S Luding. International Journal of Multiphase Flow. *International Journal of Multiphase Flow*, 37(8):956–966, October 2011.

[48] Duncan A Lockerby, Jason M Reese, and Michael A. Gallis. Capturing the Knudsen Layer in Continuum-Fluid Models of Nonequilibrium Gas Flows. *AIAA Journal*, 43(6):1391–1393, June 2005.

[49] Karen M. McNamara, Daniel J. Schneberk, Daniel M. Empey, Ajay Koshti, D. Elizabeth Pugel, Ioana Cozmuta, Malread Stackpoole, Norman P. Ruffino, Eddie C. Pompa, Ovidio Oliveras, and Dean A. Kontinos. X-Ray Computed Tomography Inspection of the Stardust Heat Shield. In *International Planetary Probe Workshop*, pages 1–12, Barcelona, June 2009.

[50] Savio Poovathingal, Thomas E Schwartzentruber, Sriram Goverapet Srinivasan, and Adri C T van Duin. Large Scale Computational Chemistry Modeling of the Oxidation of Highly Oriented Pyrolytic Graphite. *The Journal of Physical Chemistry A*, 117(13):2692–2703, April 2013.

[51] Bonnie J. McBride and Sanford Gordon. *Computer Program for Calculation of Complex Chemical Equilibrium Compositions and Applications*. NASA Lewis Resarch Center, June 1996.

[52] H. J. T. Ellingham. Reducibility of oxides and sulfides in metallurgical processes. 63(5):125–133, 1944.

[53] Francesco Panerai, Alexandre Martin, Nagi N. Mansour, Steve Sepka, and Jean Lachaud. Flow-tube Oxidation Experiments on the Carbon Preform of PICA. In *44th AIAA Thermophysics Conference*, pages 1–14, San Diego, June 2013.

[54] Y Aspa, J Lachaud, G L Vignoles, and M Quintard. Simulation of C/C composites ablation using a VOF method with moving reactive interface. *ECCM12 proceedings*, (385), 2006.

[55] J B Scoggins, N N Mansour, and H A Hassan. Development of a Reduced Kinetic Mechanism for PICA Pyrolysis Products. In *42nd AIAA Thermophysics Conference*, Honolulu, June 2011.

[56] Alexandre Martin and Iain D Boyd. Assessment of carbon-phenolic-in-air chemistry models for atmospheric re-entry. In *10th AIAA/ASME Joint Thermophysics and Heat Transfer Conference*, pages 1–15, Chicago, June 2010.

[57] Nagi N. Mansour, Francesco Panerai, Alexandre Martin, Dilworth Y Parkinson, Alastair A MacDowell, Abdelmoula Haboub, Timothy A Sandstrom, Tony Fast, Gerard L Vignoles, and Jean Lachaud. A New Approach To Light-Weight Ablators Analysis: From Micro-Tomography Measurements to Statistical Analysis and Modeling. In *44th AIAA Thermophysics Conference*, pages 1–11, San Diego, June 2013.

[58] Eric C. Stern, Ioannis Nompelis, Thomas E Schwartzentruber, and Graham V Candler. Microscale Simulations of Porous TPS Materials: Application to Permeability. In *11th AIAA/ASME Thermophysics and Heat Transfer Conference*, pages 1–14, Atlanta, June 2014.